

# Hydropathicity-Based Prediction of Pain-Causing NaV1.7 Variants

**Markos Xenakis** (✉ [markos.xenakis@maastrichtuniversity.nl](mailto:markos.xenakis@maastrichtuniversity.nl))

Maastricht University

**Dimos Kapetis**

Istituto Neurologico Carlo Besta

**Yang Yang**

Purdue University West Lafayette

**Monique Gerrits**

Maastricht University

**Jordi Heijman**

Maastricht University

**Stephen Waxman**

Yale University

**Giuseppe Lauria**

Istituto Neurologico Carlo Besta

**Catharina Faber**

Maastricht University

**Ronald Westra**

Maastricht University

**Patrick Lindsey**

Maastricht University

**Hubert Smeets**

Maastricht University

---

## Research Article

**Keywords:** NaV1.7, missense mutations, pain, atomic hydropathicity, computational modeling, cumulative hydropathic topology, scaling, pathogenicity prediction

**Posted Date:** January 7th, 2021

**DOI:** <https://doi.org/10.21203/rs.3.rs-131515/v1>

**License:**  This work is licensed under a Creative Commons Attribution 4.0 International License.

[Read Full License](#)

---

**Version of Record:** A version of this preprint was published at BMC Bioinformatics on April 23rd, 2021.  
See the published version at <https://doi.org/10.1186/s12859-021-04119-2>.

# Hydropathicity-based prediction of pain-causing NaV1.7 variants

Makros N. Xenakis<sup>a,b,\*</sup>, Dimos Kapetis<sup>c</sup>, Yang Yang<sup>d,e</sup>, Monique M. Gerrits<sup>f</sup>, Jordi Heijman<sup>g</sup>, Stephen G. Waxman<sup>h,i</sup>, Giuseppe Lauria<sup>c,j</sup>, Catharina G. Faber<sup>k</sup>, Ronald L. Westra<sup>l</sup>, Patrick J. Lindsey<sup>a,m</sup>, Hubert J. Smeets<sup>a,b</sup>

<sup>a</sup>Department of Toxicogenomics, Section Clinical Genomics, Maastricht University, PO Box 616, 6200 MD Maastricht, the Netherlands

<sup>b</sup>Research School for Mental Health and Neuroscience (MHeNS), Maastricht University, PO Box 616, 6200 MD Maastricht, The Netherlands

<sup>c</sup>Neuroalgotomy Unit, Fondazione IRCCS Istituto Neurologico "Carlo Besta", via Celoria 11, 20133 Milan, Italy

<sup>d</sup>Department of Medicinal Chemistry and Molecular Pharmacology, Purdue University College of Pharmacy, West Lafayette, IN, 47907, USA

<sup>e</sup>Purdue Institute for Integrative Neuroscience, West Lafayette, IN 47907, USA

<sup>f</sup>Department of Clinical Genetics, Maastricht University Medical Center, PO box 5800, 6202 AZ, Maastricht, the Netherlands

<sup>g</sup>Department of Cardiology, CARIM School for Cardiovascular Diseases, Maastricht University, PO Box 616, 6200 MD Maastricht, The Netherlands

<sup>h</sup>Department of Neurology and Center for Neuroscience and Regeneration Research, Yale University School of Medicine, New Haven, CT 06510, USA.

<sup>i</sup>Rehabilitation Research Center, Veterans Affairs Connecticut Healthcare System, West Haven, CT 06516, USA.

<sup>j</sup>Department of Biomedical and Clinical Sciences "Luigi Sacco", University of Milan, via G.B. Grassi 74, 20157 Milan, Italy

<sup>k</sup>Department of Neurology, Maastricht University Medical Center, PO Box 5800, 6202 AZ Maastricht, The Netherlands

<sup>l</sup>Department of Data Science and Knowledge Engineering, Maastricht University, PO Box 616, 6200 MD Maastricht, the Netherlands

<sup>m</sup>Research School for Oncology and Developmental Biology (GROW), Maastricht University, PO Box 616, 6200 MD Maastricht, the Netherlands

---

## Abstract

**Background:** Mutation-induced variations in the functional architecture of the NaV1.7 channel protein are causally related to a broad spectrum of human pain disorders. Predicting *in silico* the phenotype of NaV1.7 variant is of major clinical importance; it can aid in reducing costs of *in vitro* pathophysiological characterization of NaV1.7 variants, as well as, in the design of drug agents for counteracting adhere pain symptoms.

**Results:** In this work, we utilize spatial complexity of hydropathic effects toward predicting which NaV1.7 variants cause pain (and which are neutral) based on the location of its mutation site within the NaV1.7 structure. For that, we

---

\*Correspondence and requests for materials should be addressed to M.N.X. E-mail: mrk-sxenakis@gmail.com

analyze topological and scaling hydrophobic characteristics of the atomic environment around NaV1.7's pore and probe their spatial correlation with mutation sites. We show that pain-related mutation sites occupy structural locations in proximity to a hydrophobic patch lining the pore while clustering at a critical hydrophobic-interactions distance from the selectivity filter (SF). Taken together, these observations can differentiate pain-related NaV1.7 variants from neutral ones, i.e., NaV1.7 variants not causing pain disease, with 80.5% sensitivity and 93.7% specificity [area under the receiver operating characteristics curve = 0.872].

**Conclusions:** Our findings suggest that maintaining hydrophobic NaV1.7 interior intact, as well as, a finely-tuned (dictated by hydrophobic interactions) distance from the SF might be necessary molecular conditions for physiological NaV1.7 functioning. The main advantage for using the presented predictive scheme is its negligible computational cost, as well as, hydrophobicity-based biophysical rationalization.

*Keywords:*

NaV1.7, missense mutations, pain, atomic hydrophobicity, computational modeling, cumulative hydrophobic topology, scaling, pathogenicity prediction

---

## 1 Introduction

2 Voltage-gated sodium channels (NaVChs) are pore-forming proteins span-  
3 ning the cell membrane. They are members of the ion channels superfamily  
4 and their main physiological role is to control transport of sodium ions across  
5 cell membranes. The human NaV1.7 channel is encoded by the *SCN9A* gene  
6 and is preferentially expressed in peripheral neurons (e.g., dorsal root ganglion  
7 (DRG) nociceptors) responsible for networking pain signals. The structure of  
8 the NaV1.7  $\alpha$ -subunits is that of a pore-forming tetramer via assembly of four  
9 heterogeneous domains (DI-DIV). Three intracellular loops (L1-L3) form struc-  
10 tural interconnections among subsequent domains. Each domain comprises six  
11 transmembrane helices (S1-S6) organized into a pore module (PM) forming  
12 an ion-conduction pathway coupled with a voltage-sensor (VS). Mechanistic de-  
13 scription of NaV1.7's function is that VSs react to extracellular changes in ionic  
14 concentrations by moving outwards thus exerting a pulling force upon the PM  
15 which opens the channel pore. Closed-to-open gating transition leads to chan-  
16 nel activation, i.e., renders it conductive to sodium ions. Missense mutations in  
17 the *SCN9A* gene can destabilize the NaV1.7's functional architecture thus dis-  
18 rupting physiological gating and, consequently, deregulate flow of sodium ions  
19 through the pore. At a cellular level, these genetically-caused destabilizations  
20 can affect neuronal excitability by inducing a gain-of-function (GOF) effect, i.e.,  
21 by increasing the net ionic flow, thus triggering a wide spectrum of pain diseases  
22 such as inherited erythromelalgia (IEM) [1, 2, 3, 4, 5, 6, 7, 8, 9, 10, 11, 12, 13,  
23 14, 15, 16, 17, 18, 19, 20, 21, 22, 23, 24, 25, 26, 27, 28, 29, 30, 31], paroxysmal  
24 extreme pain disorder (PEPD) [32, 33, 34, 35, 36, 37, 38, 39] and small fiber

25 neuropathy (SFN) [40, 41, 42, 43, 44]. A proof of concept for the GOF-pain cor-  
26 relation hypothesis came from identification of missense *SCN9A*-gene mutations  
27 inducing a loss-of-function (LOF) effect, i.e., decreasing sodium-ions membrane  
28 currents, that is causally related to clinical symptoms of loss of pain sensation  
29 [45, 46, 47].

30 Hydropathic interactions (HIs) represent a summary of fundamental molec-  
31 ular interactions [48] driving molecular phenomena such as protein folding,  
32 protein hydrophobic-core stability, self-assembly of amphiphilic molecules and  
33 "dewetting" transitions occurring at the nanoscale (for a review in HIs-driven  
34 phenomena see [49]). Within the field of ion channels research, experimental  
35 and computational studies have shown that HIs are crucial regulators of gating  
36 processes occurring within the pore's microenvironment (termed as hydropho-  
37 bic gating phenomena [50]), as well as, of channel stability via formation of  
38 hydrogen bonds networks [51, 52] initiated by pore-lining hydrophobic residue  
39 patches [53]. Computational modeling of HIs combined with biophysical ob-  
40 servations extracted from *in vitro* NavCh pathophysiological characterization  
41 can propel our understanding of mechanistic linkages between mutation-induced  
42 perturbations and human pain pathophysiology. Key-studies toward this direc-  
43 tion were these of Lampert et al [54] and of Yang et al [55] demonstrating how  
44 the F1449V mutation and the in-frame-deletion L955Del, respectively, can dis-  
45 rupt a hydrophobic ring stabilizing the putative activation gate (AG) of the  
46 Nav1.7 thus acting as disease-causing molecular triggers. Moreover, computa-  
47 tional modeling successfully deduced an energetic coupling between two differ-  
48 ent IEM-related mutations foreseen by their geometrical proximity in Nav1.7  
49 structure [7]. A question that naturally arose from these studies was whether a  
50 detailed examination of HIs network characteristics within a Nav1.7 structure  
51 can reveal statistically-significant but also biophysically-relevant differentiations  
52 among the WT structure and its variants. This question was probed by Kapetis  
53 et al [56]; a network-theoretical computational framework was introduced in  
54 order to capture changes in inter-atomic HIs within a Nav1.7 WT structure  
55 induced by pain-related mutations. The study reported on a betweenness cen-  
56 trality network measure achieving a statistically-important differentiation of  
57 pain-related variants from a collection of neutrals, i.e., variants not causing  
58 pain disease. Notably, this approach highlighted the prominent role that HIs  
59 play in Nav1.7's stability and reported on plausible mutation-mechanism sce-  
60 narios disrupting hydrophobic contacts among neighboring and distant residues.  
61 Another remark on the multi-scale nature of HIs was made by the authors of  
62 [57] suggesting that a pathogenic mutation in the *KCNA1* gene encoding the  
63 human voltage-gated potassium channel KV1.1 can de-tune HIs equilibrium  
64 (and, consequently, destabilize KV1.1's pre-open conformation) implying that  
65 mutation-induced perturbation effects can destroy finely-tuned network-like HIs  
66 expanding throughout the structure as a whole. Interestingly, the fine-tuning  
67 hypothesis was proposed also for the Nav1.7; a recent study employing a ma-  
68 chine learning (MLE) computational pipeline for predicting Nav1.7's variant  
69 pathogenicity suggested that the fine-tuning of the Nav1.7 channel is so deli-  
70 cate that limits classification accuracy of practically any computational ap-

71 proach [97]. Taken together, these observations highlight the highly-cooperative  
72 nature of HIs [48] and suggest that even small changes in the hydrophobic spa-  
73 tial distribution profile of a channel structure can have a detrimental impact  
74 on the functional architecture which, in turn, might induce clinically-observed  
75 alterations of electrophysiology.

76 Following [56, 97], this study aims at probing the finely-tuned hypothesis  
77 for the NaV1.7’s atomic hydrophobic environment in order to predict whether  
78 a NaV1.7 variant causes pain or not. We utilize a closed-state structural model  
79 of the NaV1.7 retrieved from homology modeling based on the pre-open NaVAb  
80 [58] template (first presented in [55] and later used also in [7]) and investigate  
81 cumulative, i.e., scale-dependent, hydrophobic properties of its porous atomic en-  
82 vironment in relation to structural locations of missense *SCN9A*-gene mutations.  
83 In order to tackle spatial complexities emerging from the highly-cooperative na-  
84 ture of HIs we adopt a modeling approach rooted in the hypothesis that proteins  
85 can be represented as self-organized criticality (SOC) [59] archetypes; protein  
86 structures are thought to have been evolutionary optimized with respect to ex-  
87 tremity in some thermodynamic property (or properties) capturing a qualitative  
88 reorganization of the atomic environment [60, 61]. The intra-channel locations  
89 where these macroscopic thermodynamic changes take place correspond to so-  
90 called critical points of the atomic structure [60, 61]. The highly-cooperative na-  
91 ture of HIs has placed structure-retrieved hydrophobic properties in the epicenter  
92 of SOC hypothesis [60, 61, 62, 63]). It is important to note that computational  
93 evidence for a universal hydrophobic-to-hydrophilic (or inside-outside with ”in-  
94 side” referring to the hydrophobic core and ”outside” referring to the hydrophilic  
95 exterior) spatial transition in protein systems was first provided before the for-  
96 mulation of the SOC hypothesis (see [64]). Departing from this phenomenologi-  
97 cal basis, we here utilize the finite-size scaling analysis methodologies presented  
98 in [65, 66] for screening hydrophobic morphology around NaV1.7’s pore [65]  
99 toward identification of critical points associated with NaV1.7’s functional ar-  
100 chitecture. Biophysical relevance of retrieved observations is justified not only  
101 in terms of the scale-invariance of a carefully-chosen cumulative hydrophobicity-  
102 property function but also with respect to conserved structural NaV1.7 features  
103 such as the PM-VSs spatial transition and the location of the selectivity filter  
104 (SF). In particular, we demonstrate that the atomic cumulative distribution  
105 function around NaV1.7’s pore exhibits a sigmoid profile with inflection points  
106 matching closely the conserved PM-VSs spatial transition. This provides a rigor  
107 description of atom-packing geometry and, consequently, a macroscopic parti-  
108 tioning of the atomic environment around the pore allowing for mapping the  
109 spatial profile of the atomic cumulative hydrophobicity-property function and  
110 mutation sites on two dimensions. The SOC hypothesis is then accepted (or  
111 rejected) depending on whether the cumulative hydrophobicity-property func-  
112 tion is globally maximized and exhibits power-law-like scaling behavior in the  
113 vicinity of the inflection point (or not).

114 Our mapping procedures reveal the formation of a hydrophobic patch (HP)  
115 incorporating NaV1.7’s central cavity (CC) and activation gate (AG). We report  
116 on two ”hot” map areas attracting pain-related mutation sites which are dis-

117 tributed either inside or along HP’s periphery. Probing the SOC hypothesis for  
 118 the NaV1.7 structure reveals that ”hot” structural locations tend to cluster at a  
 119 distance of 33.4 Å from the SF. Stability implications of these observations can  
 120 be concertized by considering that in the vicinity of the critical point the range  
 121 and intensity of HIs increase in a power-law fashion thus favoring amplification  
 122 and propagation of mutation-induced perturbations only peripherally to the HP  
 123 and at critical HIs-distance from the SF thus not directly affecting neither of  
 124 them. The clinical translational value of our findings is tested by predicting  
 125 pathogenicity of 84 NaV1.7 variants; a weighted average of HP- and SF-related  
 126 distance metrics can classify up to 29 (out of 36) pain-related variants and 45  
 127 (out of 48) neutral variants correctly.

## 128 **Methods**

129 All computations were performed in R [67] environment unless stated differ-  
 130 ently.

### 131 *3D structure preparation*

132 We fetch the NaV1.7 atomic structure model constructed via homology mod-  
 133 eling procedures based on the pre-open NaVAAb [58] template (for model con-  
 134 struction details see [7]). Its principal axes were estimated by using the VMD  
 135 software [68]. A global coordinate system ( $\hat{\mathbf{x}}, \hat{\mathbf{y}}, \hat{\mathbf{z}}$ ) was introduced with its cen-  
 136 ter at  $O$  and the NaV1.7’s principal pore axis, i.e., the axis approximating the  
 137 direction of the channel’s pore, was aligned with the  $z$ -axis with orientation from  
 138 the extracellular side (ES) toward the intracellular side (IS) with respect to  $\hat{\mathbf{z}}$ .  
 139 The atomic center  $\mathbf{e} = \frac{1}{M} \sum_{i=1}^{N_c} m_i \cdot \mathbf{c}_i$  of the 3D structure was set to overlap with  
 140  $O$ , where  $\mathbf{c}_i = (c_{x,i}, c_{y,i}, c_{z,i})$  is the atomic center of the  $i$ -th atom,  $m_i$  is the mass  
 141 of the  $i$ -th atom,  $N_c = 18567$  is the total number of atoms and  $M = \sum_{i=1}^{N_c} m_i$  is  
 142 the total molecular mass (values of atomic masses are the same as [? ?]).

### 143 *Geometrical characteristics of the pore*

144 We navigated through the skewed NaV1.7’s pore by introducing pore points  
 145  $\mathbf{p}$  (see Supplementary Material (SM), S1). The pore radius at  $\mathbf{p}$  is given by [72]

$$R(\mathbf{p}) = \min_{i=1,2,\dots,N_c} \{ \|\mathbf{c}_i - \mathbf{p}\| - vdW_i \} \quad (\text{m2})$$

146 where  $\|\cdot\|$  is the euclidean norm and  $vdW_i$  is the van der Waals radius of the  
 147  $i$ -th atom (values of van der Waals radii are the same as [? ?]). The distance  
 148 between  $\mathbf{p}$  and its nearest neighbor atom corresponds then to

$$D(\mathbf{p}) = \min_{i=1,2,\dots,N_c} \{ \|\mathbf{c}_i - \mathbf{p}\| \} \quad (\text{m3})$$

149 and the outer surface radius at  $\mathbf{p}$  is given by [65, 66]

$$L(\mathbf{p}) = \max_{i=1,2,\dots,N_c} \{ \|\mathbf{c}_i - \mathbf{p}\| + vdW_i \} \quad (\text{m4})$$

150 where the unit of measurement for  $R(\mathbf{p})$ ,  $D(\mathbf{p})$  and  $L(\mathbf{p})$  is expressed in [Å].

151 *Finite-size sampling around the pore*

152 The atomic environment around  $\mathbf{p}$  is sampled with concentric spheres placed  
153 at  $\mathbf{p}$  of increasing radius [65, 66]

$$l_\alpha(\mathbf{p}) = D(\mathbf{p}) + \alpha \cdot \frac{L(\mathbf{p}) - D(\mathbf{p})}{K_\alpha} \text{ for } \alpha = 1, 2, \dots, K_\alpha \rightarrow \infty \quad (\text{m5})$$

154 where  $K_\alpha$  is the total number of sampling spheres and  $\alpha$  denotes the index of the  
155 sampling sphere.  $l_\alpha(\mathbf{p})$  indicates the size, i.e., molecular scale, of the spherical  
156 cluster of atoms around  $\mathbf{p}$  in [ $\text{\AA}$ ] and  $L(\mathbf{p})$  the finite channel size measured with  
157 respect to  $\mathbf{p}$ . Accordingly, the atomic cumulative distribution function (CDF)  
158 at  $\mathbf{p}$  is given by [65, 66]

$$N(\mathbf{p}, l_\alpha(\mathbf{p})) = \sum_{i=1}^{N_c} \theta(l_\alpha(\mathbf{p}) - \|\mathbf{c}_i - \mathbf{p}\|) \quad (\text{m6})$$

159 where  $\theta(\cdot)$  is the heaviside function. Note that  $N(\mathbf{p}, l_\alpha(\mathbf{p}))$  essentially describes  
160 how atoms are packed around  $\mathbf{p}$ . In computational practice  $K_\alpha$  is set to be  
161 "large enough" approximating the continuous case via dense sampling.

162 *Mathematical modeling of atomic accumulation*

163 Modeling of the CDF was performed by employing the GROFIT routine [73].  
164 A collection of candidate models including re-parametrized algebraic forms [74]  
165 of the Logistic model [75]

$$n_{LOG}(\mathbf{p}, l_\alpha(\mathbf{p})) = A(\mathbf{p}) \cdot \left\{ 1 + \exp\left(\frac{4 \cdot t(\mathbf{p})}{A(\mathbf{p})} \cdot (s(\mathbf{p}) - l_\alpha(\mathbf{p})) + 2\right) \right\}^{-1} \quad (\text{m7})$$

166 , of the Gompertz model [76]

$$n_{GOM}(\mathbf{p}, l_\alpha(\mathbf{p})) = A(\mathbf{p}) \cdot \exp\left(-\exp\left(\frac{e \cdot t(\mathbf{p})}{A(\mathbf{p})} \cdot (s(\mathbf{p}) - l_\alpha(\mathbf{p})) + 1\right)\right) \quad (\text{m8})$$

167 with  $e = \exp(1)$ , of the the modified Gompertz model [77]

$$\begin{aligned} n_{MGOM}(\mathbf{p}, l_\alpha(\mathbf{p})) = & A(\mathbf{p}) \cdot \exp\left(-\exp\left(\frac{e \cdot t(\mathbf{p})}{A(\mathbf{p})} \cdot (s(\mathbf{p}) - l_\alpha(\mathbf{p})) + 1\right)\right) \\ & + A(\mathbf{p}) \cdot \exp(w(\mathbf{p}) \cdot (l_\alpha(\mathbf{p}) - l_{shift}(\mathbf{p}))) \end{aligned} \quad (\text{m9})$$

168 and of the Richards model [78]

$$\begin{aligned} n_{RIC}(\mathbf{p}, l_\alpha(\mathbf{p})) = & A(\mathbf{p}) \cdot \left\{ 1 + \tilde{q}(\mathbf{p}) \cdot b(\mathbf{p}) \cdot \exp(-k(\mathbf{p}) \cdot l_\alpha(\mathbf{p})) \right\}^{-1/\tilde{q}(\mathbf{p})} \\ \text{with } b(\mathbf{p}) = & \exp(1 + \tilde{q}(\mathbf{p}) + k(\mathbf{p}) \cdot s(\mathbf{p})) \text{ and } k(\mathbf{p}) = \frac{t(\mathbf{p})}{A(\mathbf{p})} \cdot (1 + \tilde{q}(\mathbf{p}))^{1+1/\tilde{q}(\mathbf{p})} \end{aligned} \quad (\text{m10})$$

169 were fitted on  $N(\mathbf{p}, l_\alpha(\mathbf{p}))$  along  $l_\alpha(\mathbf{p})$ -direction where  $\{A(\mathbf{p}), t(\mathbf{p}), s(\mathbf{p}), \tilde{q}(\mathbf{p}), w(\mathbf{p}), l_{shift}(\mathbf{p})\}$   
170 are model parameters. The mathematical model that best fitted  $N(\mathbf{p}, l_\alpha(\mathbf{p}))$

171 traces along  $l_\alpha(\mathbf{p})$ -direction was selected based on minimization of an Akaike  
 172 information criterion (see [73] for algorithmic details).

173 Following [66], model parameters interpretation was performed with respect  
 174 to the inflection point

$$\xi(\mathbf{p}) = \{l_\alpha(\mathbf{p}) \mid \frac{\partial^2 n(\mathbf{p}, l_\alpha(\mathbf{p}))}{\partial l_\alpha(\mathbf{p})^2} = 0\} \quad (\text{m11})$$

175 that determines the location along  $l_\alpha(\mathbf{p})$ -direction where the radial distribution  
 176 function (RDF),  $\frac{\partial n(\mathbf{p}, l_\alpha(\mathbf{p}))}{\partial l_\alpha(\mathbf{p})}$ , maximizes. The RDF maximum value is given by  
 177 the parameter  $t(\mathbf{p})$  accounting for the maximum atomic accumulation rate (or,  
 178 equivalently, for the maximum atomic density) around  $\mathbf{p}$ . Parameter  $A(\mathbf{p})$  is  
 179 the asymptote value of the fitted model, i.e.,  $n(\mathbf{p}, l_\alpha(\mathbf{p}) \rightarrow \infty) = A(\mathbf{p})$ , describing  
 180 what happens when  $L(\mathbf{p})$  becomes arbitrary large. Parameter  $s(\mathbf{p})$  determines  
 181 the location along  $l_\alpha(\mathbf{p})$ -direction where the lag domain ends, i.e., the size of the  
 182 lag atomic accumulation domain. Interpretation of parameter  $t(\mathbf{p})$  is retrieved  
 183 in terms of the ratio  $t(\mathbf{p}) = \frac{A(\mathbf{p})}{os(\mathbf{p})=o(\mathbf{p})-s(\mathbf{p})}$  with  $o(\mathbf{p})$  determining the location  
 184 along  $l_\alpha(\mathbf{p})$ -direction where the asymptote atomic accumulation domain begins.  
 185 Parameter  $\tilde{q}(\mathbf{p})$  affects the shape of the Richards model curve, as well as, the  
 186 location of the inflection point along  $l_\alpha(\mathbf{p})$ -direction thus plays the role of the  
 187 summary atom-packing parameter. Parameters  $w(\mathbf{p})$  and  $l_{shift}(\mathbf{p})$  of the mod-  
 188 ified Gompertz model indicate the location and the slope, respectively, of a  
 189 second increase in the modified Gompertz model curve (see [73]). The Logistic  
 190 and the Gompertz model are retrieved from the Richards model for  $\tilde{q}(\mathbf{p}) = 1$   
 191 and  $\tilde{q}(\mathbf{p}) \rightarrow 0$ , respectively, as shown in [79], thus they are considered as special  
 192 cases of the Richards model.

### 193 *Cumulative hydropathicity-property functions*

194 The hydropathic density of the atomic environment around  $\mathbf{p}$  was approxi-  
 195 mated in terms of [65]

$$m^{(0)}(\mathbf{p}, l_\alpha(\mathbf{p})) = \frac{h^{(0)}(\mathbf{p}, l_\alpha(\mathbf{p}))}{N(\mathbf{p}, l_\alpha(\mathbf{p}))} \sim kcal/(mol \equiv atom) \quad (\text{m12})$$

$$\text{with } h^{(0)}(\mathbf{p}, l_\alpha(\mathbf{p})) = \sum_{i=1}^{N_c} \theta(l_\alpha(\mathbf{p}) - \|\mathbf{c}_i - \mathbf{p}\|) \cdot HI_i^w$$

196 where  $h^{(0)}(\mathbf{p}, l_\alpha(\mathbf{p}))$  corresponds to the cumulative zero-order hydropathic pore  
 197 moment function [80] with  $HI_i^w = HI_i + w_i$  representing the  $i$ -th atomic hy-  
 198 drophobic index in accordance with the corrected Kapcha-Rosky atomic hy-  
 199 drophobic scale presented in [65] (note that the Kapcha-Rosky atomic hy-  
 200 drophobic scale was initially published in [81] where a HIS atom was missing  
 201 and was later added in [65]) with additive gaussian noise  $w_i \in \mathcal{N}(\mu=0, \sigma=0.001)$ .  
 202 The superscript "(0)" indicates the moment order.

203 The hydropathic inter-atomic interaction strength (HIIS) at  $\mathbf{p}$ , i.e., the aver-  
 204 age interaction strength between an atomic component found within the cluster

205 of size  $N(\mathbf{p}, l_\alpha(\mathbf{p}))$  and its surroundings, was approximated in terms of the hy-  
 206 dropathic imbalance (or interaction strength) pore function [65, 66]

$$\begin{aligned} \vec{\mathbf{m}}^{(1)}(\mathbf{p}, l_\alpha(\mathbf{p})) &= \frac{\vec{\mathbf{h}}^{(1)}(\mathbf{p}, l_\alpha(\mathbf{p}))}{N(\mathbf{p}, l_\alpha(\mathbf{p}))} \sim kcal \cdot \text{\AA} / (mol \equiv atom) \\ \text{with } \vec{\mathbf{h}}^{(1)}(\mathbf{p}, l_\alpha(\mathbf{p})) &= \sum_{i=1}^{N_c} \theta(l_\alpha(\mathbf{p}) - \|\mathbf{c}_i - \mathbf{p}\|) \cdot HI_i^w \cdot \vec{\mathbf{r}}_{\mathbf{p},i} \\ &= \underbrace{h_x^{(1)}(\mathbf{p}, l_\alpha(\mathbf{p})) \cdot \hat{\mathbf{x}} + h_y^{(1)}(\mathbf{p}, l_\alpha(\mathbf{p})) \cdot \hat{\mathbf{y}}}_{\vec{\mathbf{h}}_{xy}^{(1)}(\mathbf{p}, l_\alpha(\mathbf{p}))} + \underbrace{h_z^{(1)}(\mathbf{p}, l_\alpha(\mathbf{p})) \cdot \hat{\mathbf{z}}}_{\vec{\mathbf{h}}_z^{(1)}(\mathbf{p}, l_\alpha(\mathbf{p}))} \end{aligned} \quad (\text{m13})$$

207 where  $\vec{\mathbf{h}}^{(1)}(\mathbf{p}, l_\alpha(\mathbf{p}))$  corresponds to cumulative first-order hydrophatic pore mo-  
 208 ment function [80] quantifying the hydrophatic inter-cluster interaction strength  
 209 (HIcIS) with  $\vec{\mathbf{r}}_{\mathbf{p},i}$  being the vector from  $\mathbf{p}$  to  $\mathbf{c}_i$ . The superscript "(1)" indicates  
 210 the moment order.

211 Introduction of the weak noise source  $w_i$  practically guarantees that  $|h^{(0)}(\mathbf{p}, l_\alpha(\mathbf{p}))|$   
 212 and  $|\vec{\mathbf{h}}^{(1)}(\mathbf{p}, l_\alpha(\mathbf{p}))|$  are non-zero for every combination of  $\mathbf{p}$  and  $l_\alpha(\mathbf{p})$  while  
 213 their scaling behavior remains practically unaffected. Throughout this study we  
 214 consider pore's physicochemical field characteristics to be adequate described  
 215 in terms of the axial component,  $\vec{\mathbf{m}}_z^{(1)}(\mathbf{p}, l_\alpha(\mathbf{p})) = \vec{\mathbf{h}}_z^{(1)}(\mathbf{p}, l_\alpha(\mathbf{p})) / N(\mathbf{p}, l_\alpha(\mathbf{p})) =$   
 216  $m_z^{(1)}(\mathbf{p}, l_\alpha(\mathbf{p})) \cdot \hat{\mathbf{z}}$  given that the magnitude of the radial component,  $\|\vec{\mathbf{m}}_{xy}^{(1)}(\mathbf{p}, l_\alpha(\mathbf{p}))\| =$   
 217  $\|\vec{\mathbf{h}}_{xy}^{(1)}(\mathbf{p}, l_\alpha(\mathbf{p}))\| / N(\mathbf{p}, l_\alpha(\mathbf{p}))$ , is vanishingly small relative to  $\|\vec{\mathbf{m}}^{(1)}(\mathbf{p}, l_\alpha(\mathbf{p}))\|$   
 218 after a cut-off, lag-domain scale (see SM, S2). Hence, we focus throughout  
 219 this study only on the scaling behavior and topology of the HIIS axial field  
 220 component which can occupy only two states; an "in" state which is charac-  
 221 terized by  $\vec{\mathbf{m}}_z^{(1)}(\mathbf{p}, l_\alpha(\mathbf{p}))$  pointing towards the intracellular side (IS), i.e., by  
 222  $m_z^{(1)}(\mathbf{p}, l_\alpha(\mathbf{p})) > 0$ , and an "out" state which is characterized by  $\vec{\mathbf{m}}_z^{(1)}(\mathbf{p}, l_\alpha(\mathbf{p}))$   
 223 pointing towards the extracellular side (ES), i.e., by  $m_z^{(1)}(\mathbf{p}, l_\alpha(\mathbf{p})) < 0$ . Topo-  
 224 logical changes in HIIS axial field component are detected according to the  
 225 algorithmic scheme presented in [65] (see SM, S3).

### 226 *Finite-size scaling of HIIS*

227 In accordance to [66], a scale-invariant interval of the HIIS axial component  
 228 corresponds to combinations of  $\mathbf{p}$  with  $\alpha$  for which the power-law approximation

$$\|\vec{\mathbf{m}}_z^{(1)}(\mathbf{p}, l_\alpha(\mathbf{p}))\| \sim l_\alpha(\mathbf{p})^{\gamma(\mathbf{p})} \quad (\text{m14})$$

229 is accurately satisfied indicating that HIIS stabilizing the cluster of  $N(\mathbf{p}, l_\alpha(\mathbf{p}))$   
 230 atoms around  $\mathbf{p}$  span a range up to  $\sim l_\alpha(\mathbf{p}) \text{\AA}$ . Sign of  $\gamma(\mathbf{p})$  quantifies the  
 231 rate at which intensity and range of HIIS increase or decrease for increasing  
 232 atomic cluster size. From a HIs-network standpoint,  $\gamma(\mathbf{p})$  indicates whether HIs  
 233 network interconnectivity is up- or down-regulated, i.e., whether HIs bonds, e.g.,  
 234 hydrogen bonds, are created or destroyed within the structure. The energy levels

235 associated with HIs bonds formation (or de-formation) guaranteeing stability of  
236 the atomic cluster can then be approximated by

$$U(\mathbf{p}, l_\alpha(\mathbf{p})) := \|\vec{h}_z^{(1)}(\mathbf{p}, l_\alpha(\mathbf{p}))\|/l_\alpha(\mathbf{p}) \sim N(\mathbf{p}, l_\alpha(\mathbf{p})) \cdot l_\alpha(\mathbf{p})^{\gamma(\mathbf{p})-1} \quad (\text{m15})$$

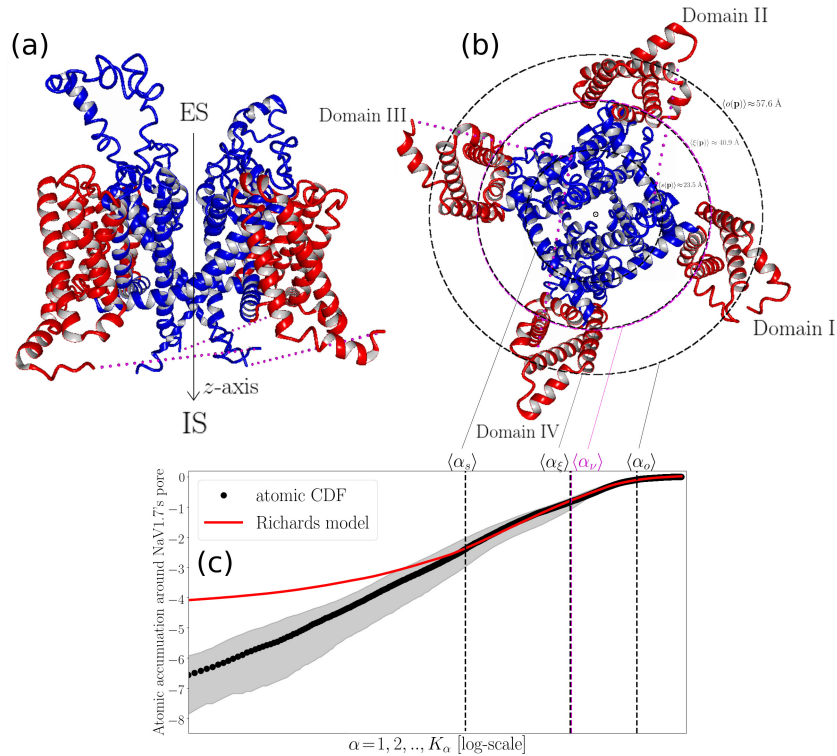
237 measured in kcal/(mol $\equiv$ atomic cluster).

## 238 Results

239 In Figure 1 we demonstrate that atomic accumulation around NaV1.7's pore  
240 follows a sigmoid profile which can be accurately described by the Richards  
241 model (SM, S4). Inflection behavior of atomic accumulation can thus be de-  
242 scribed in terms of the inflection points,  $\xi(\mathbf{p})$ , so that the atomic environment  
243 around the pore is partitioned into four consecutive domains spanning NaV1.7  
244 from the inside to the outside (Figure 1(b),(c)). Structural locations of the  
245 inflection points correspond to intra-channel regions where the atomic density  
246 maximizes and were found to closely follow the PMs-VSs spatial transition (see  
247 SM, S5 for calculation of PMs-VSs spatial transition characteristics). Accord-  
248 ingly,  $\xi(\mathbf{p})$  serves as a macroscopic boundary line splitting the atomic environ-  
249 ment around NaV1.7's pore into two phases, namely, a pre-inflection phase for  
250  $l_\alpha(\mathbf{p}) \leq \xi(\mathbf{p})$  and a post-inflection phase for  $l_\alpha(\mathbf{p}) > \xi(\mathbf{p})$  accounting for atomic  
251 sub-environments containing mainly structural components belonging to the  
252 PMs and VSs, respectively (Figure 1(b)).

253 Based on the geometrical partition scheme summarized in Figure 1 we pro-  
254 ceeded with mapping of missense *SCN9A*-gene mutation intra-channel structural  
255 locations. For that, we utilized a set of well-studied GOF NaV1.7 mutations  
256 prototypically related with IEM, SFN and PEPD pain disease (total number  
257 of pain-related mutation sites: 36) and a set of neutral NaV1.7 mutations, i.e.,  
258 NaV1.7 variants not causing disease, (total number of neutral mutations: 48)  
259 and retrieved their corresponding two-dimensional map site (SM, S7).

260



261

262 **Figure 1: Atomic accumulation around NaV1.7's pore.** (a),(b) Cartoon illustration of the NaV1.7 human channel (side and top views). The atomic environment  
 263 around the pore is partitioned into three consecutive domains; a lag domain, an inflection  
 264 domain, and an asymptote domain. The upper boundaries of the lag domain, of  
 265 the pre-inflection domain and of the post-inflection domain are also shown in terms of  
 266 their statistical representations  $\langle \alpha_s \rangle$ ,  $\langle \alpha_\xi \rangle$ ,  $\langle \alpha_\xi \rangle \approx \langle \alpha_\nu \rangle$  and  $\langle \alpha_o \rangle$ , respectively. Helical  
 267 structures in (a),(b) forming the PMs and the VSs are colored with red and blue color,  
 268 respectively. (c), Traces of statistical representations of the normalized (with respect to  
 269  $N_c$ ) atomic CDF,  $\langle \bar{N}(\mathbf{p}, l_\alpha(\mathbf{p})) \rangle_\alpha$ , and of its best-fitted Richards model  $\langle n(\mathbf{p}, l_\alpha(\mathbf{p})) \rangle_\alpha$   
 270 are plotted in log-scale with shaded areas around  $\langle N(\mathbf{p}, l_\alpha(\mathbf{p})) \rangle_\alpha$  indicative of 95% confi-  
 271 dence intervals. Statistical representations of scalars are calculated according to SM,  
 272 S6.  
 273

274

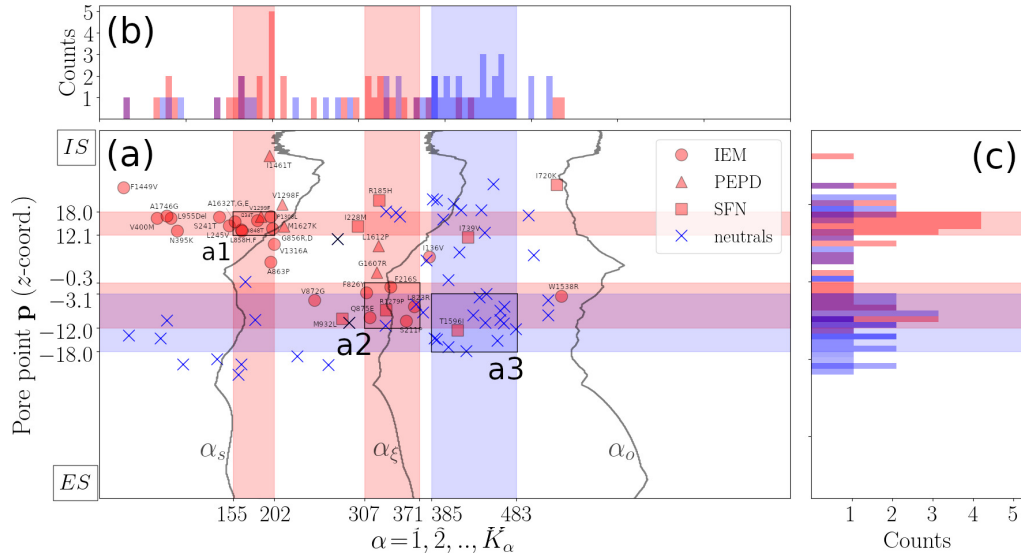
275 The majority (i.e., 54%) of pain-related mutations sites are sparsely distributed  
 276 within the inflection domain attracted and, more precisely, attracted  
 277 toward a centrally-located map area in the vicinity of the inflection-points line  
 278  $\alpha_\xi$  (see area II on Figure 2(a) in relation to Figures 2(b),(c)). On the other hand,  
 279 the majority (i.e., 75%) of neutral mutation sites are distributed within  
 280 the second part of the inflection domain so their map density tends to maximize  
 281 approximately in the middle of the second part of the inflection domain (see area  
 282 III on Figure 2(a) in relation to Figures 2(b),(c)). The rest 46% of pain-related  
 283 mutation sites are found within the lag domain toward the intracellular side of

284 the NaV1.7. In particular, their map density maximizes in the vicinity of the  
 285 boundary line  $\alpha_s$  toward the IS (see area I on Figure 2(a) in relation to Figures  
 286 2(b),(c)). Taken together, these observations indicate that for decreasing molec-  
 287 ular scale the probability of a missense *SCN9A*-gene mutation to translate into a  
 288 pain-related phenotype increases which is of little surprise considering that muta-  
 289 tions affecting NaV1.7’s interior are more likely to perturb packing of S5-S6  
 290 pore-forming helices and, consequently, affect pore’s gating behavior.

291 Mapping of hydrophathic density profile reveals the formation of a large HP  
 292 incorporating the central cavity (CC) and the AG (Figure 3). Specifically, we  
 293 demonstrate that the center of the pore is lined by predominantly hydropho-  
 294 bic atomic components expanding toward the IS where occlusion of the pore  
 295 takes place by the ring of Y405 (DI), F960 (DII) F1449 (DIII) and F1752 (DIV)  
 296 residues which are known to form the NaV1.7’s activation gate (AG) (Figure  
 297 3). Macroscopically, the wide CC translates into a structural contraction event  
 298 as the outer surface radius is locally minimized so that the channel is split  
 299 into two funnel-like structural compartments (see trace of  $L(\mathbf{p})$  on Figure 3).  
 300 Hydrophathic density variations can be summarized in terms of three visually-  
 301 distinguishable contour domains; the  $T_2^{(0)}$  domain accounting for HP’s forma-  
 302 tion, the  $T_1^{(0)}$  domain accounting for a hydrophobic pore wall placed between  
 303 the hydrophilic selectivity filter (SF) and the hydrophilic extracellular side (ES),  
 304 and the hydrophilic  $T_3^{(0)}$  domain covering the largest contour map area and in-  
 305 corporating both the SF and the ES mouth.

306

307



308

309 **Figure 2: Geometrical mapping of missense *SCN9A*-gene mutation sites.** (a),  
 310 Two sets of missense *SCN9A*-gene mutation are employed; a pain-related set contain-  
 311 ing IEM, PPD and SFN mutation sites and a neutral set containing mutation sites

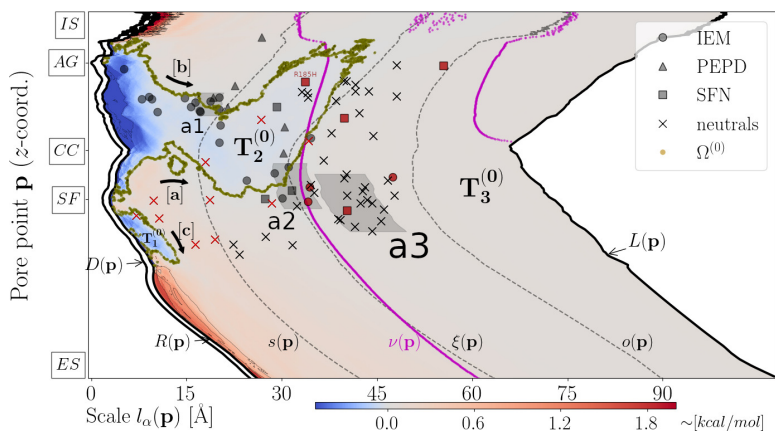
312 not related to pain disease (SM, S3). Lines  $\alpha_s$ ,  $\alpha_\xi$  and  $\alpha_o$  highlight the boundaries  
 313 among consecutive domains. Map areas "a1", "a2" and "a3" indicate maximizations  
 314 in density of mutation sites. (b), Histogram of mutation sites along  $\alpha$ -direction. (c),  
 315 Histogram of mutation sites along  $\mathbf{p}$ -direction. Red- and blue-colored histograms ac-  
 316 count for distribution of pain-related and neutral mutation sites, respectively.

317

318 The SF's microenvironment is formed by the residues D361 (DI), E930 (DII),  
 319 K1406 (DIII) and A1698 (DIV) where a bare sodium ion of radius  $\approx 1.8 \text{ \AA}$  can  
 320 exactly fit in (Figure 3). Strikingly, approximately 53% of pain-related mutation  
 321 sites are found within  $T_2^{(0)}$  while map areas I and II are distributed along HP's  
 322 boundary, i.e., occupy contour map area that belongs to both domains  $T_2^{(0)}$  and  
 323  $T_3^{(0)}$  (Figure 3). On the other hand, only 10% of neutral mutations sites are  
 324 located within the  $T_2^{(0)}$  while area III is distributed solely within  $T_3^{(0)}$  (Figure  
 325 3).

326 Given that mutations affecting a protein's hydrophobic interior pose a high  
 327 risk for detrimental destabilizations [82, 83], we hypothesize that mutations  
 328 occurring at structural locations in proximity to HP are more likely to be re-  
 329 lated with pain phenotype as their perturbing effect can directly affect tight  
 330 hydrophobic packing around channel's mass center. We test this hypothesis by  
 331 calculating the distance between each mutation structural location and HP's  
 332 boundary (SM, S8) and fed retrieved distances into a binary classifier. We  
 333 achieved to classify correctly 29 (out of 36) and 38 (out of 48) of pain-related  
 334 and neutral, respectively, mutations correctly with a cut-off distance of 18.13  
 335  $\text{\AA}$  (Figure 4). This translates to an area under receiver operating characteristics  
 336 (ROC) curve of 0.787 and pain phenotype prediction with specificity of 0.791  
 337 and sensitivity of 0.805 (Figure 4(a)).

338



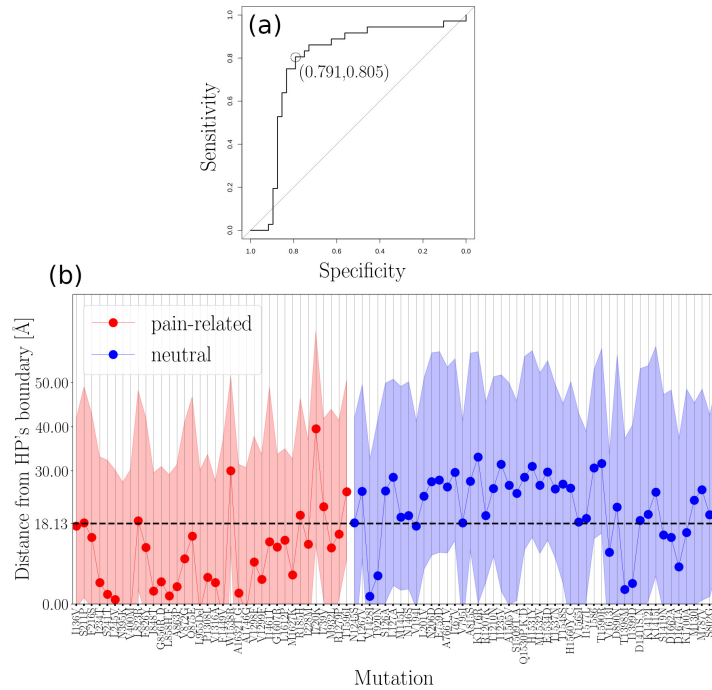
339

340 **Figure 3: Spatial profile of the hydrophobic density around NaV1.7's pore.**  
 341 Contour map of the hydrophobic density pore function,  $m^{(0)}(\mathbf{p}, l_\alpha(\mathbf{p}))$ , for  $\mathbf{p} \in P$  and  
 342  $\alpha = 1, 2, \dots, K_\alpha = 800$ . Blue and red color contour domains represent hydrophobic and  
 343 hydrophilic domains around the pore, respectively. Black lines  $R(\mathbf{p})$ ,  $\bar{R}(\mathbf{p})$  and  $L(\mathbf{p})$

344 depict geometrical pore characteristics. Magenta dashed line  $\nu(\mathbf{p})$  represents the PMS-  
 345 VSs spatial transition. Dashed black lines  $s(\mathbf{p})$ ,  $\xi(\mathbf{p})$  and  $o(\mathbf{p})$  account for the bound-  
 346 aries between different domains (see Methods). Zero-crossing points of  $m^{(0)}(\mathbf{p}, l_\alpha(\mathbf{p}))$   
 347 collected in  $\Omega^{(0)}$  describe the boundaries among hydrophobic domains  $T_1^{(0)}$ ,  $T_2^{(0)}$  and  
 348  $T_3^{(0)}$ . Pain-related and neutral mutation sites are represented by different symbols (see  
 349 Legend). Mutations sites highlighted with red color correspond to misclassified events.  
 350 Grey-shaded areas "a1", "a2" and "a3" highlight map areas where map density of mu-  
 351 tation sites maximizes.

352  
 353 Misclassified pain-related mutations S211P, L823R, W1538R, I720K, I739V  
 354 and T1596I are found outside of  $T_2^{(0)}$  thus not in proximity to HP (Figure 3 and  
 355 4(b)). Only a single pain-related misclassification is found within  $T_2^{(0)}$ , namely,  
 356 R185H (Figure 3 and 4(b)). This striking misclassification is due to the ele-  
 357 mentary statistical approach adopted for calculating distance scores which fails to  
 358 capture the complex geometry of  $T_2^{(0)}$  (SM, S8). Misclassified neutral muta-  
 359 tions are V1428I, T920N, V194I, V1613I, T1398N, I1399D, S1419N, D1662A,  
 360 D1674A and K1700A are found either inside  $T_2^{(0)}$  or in close proximity to HP's  
 361 boundary with a tendency to cluster around the SF (Figure 3 and 4(b)).

362



363

364 **Figure 4: Binary classification of NaV1.7 variants based on their distance**  
 365 **from the HP's boundary.** (a), ROC curve constructed based on the HP's-boundary  
 366 distance data (for construction of data set see SM, S8). Optimal threshold value cor-  
 367 responds to specificity and sensitivity values of 0.791 and 0.805, respectively. Area under

368 ROC curve is 0.787. (b), Visualization of ROC curve data. Optimal threshold value  
 369 18.13 Å is marked with black dashed line. Shaded area around distance values indicates  
 370 the 95% confidence intervals. ROC curve is constructed in R [67] by using the pROC  
 371 package [84].

372

373 HIs underlying atom packing around NaV1.7's pore can be adequately de-  
 374 scribed in terms of the HIIS axial field component illustrated in Figure 5(a).  
 375 HIIS axial field topology is organized into five domains, namely, of  $T_1^{(1)}$ ,  $T_2^{(1)}$ ,  
 376  $T_3^{(1)}$ ,  $T_4^{(1)}$  and  $T_5^{(1)}$  (Figure 5(a)). The centrally-located  $T_5^{(1)}$  domain covers the  
 377 largest map area and roughly dichotomizes the contour map into two pseudo-  
 378 symmetric parts, namely, an ES part incorporating  $T_1^{(1)}$  and  $T_3^{(1)}$  an IS part  
 379 incorporating  $T_2^{(1)}$  and  $T_4^{(1)}$ . Pain-related mutation sites are solely found within  
 380 the  $T_4^{(1)}$  (58%) and  $T_5^{(1)}$  (42%) domains. On the other hand, neutral sites are  
 381 found within the  $T_3^{(1)}$  (14%),  $T_4^{(1)}$  (19%) and  $T_5^{(1)}$  (67%) domains.

382 In order to decode mutation sites clustering behavior on the contour map of  
 383 Figure 5(a) we adopted a phenomenological perspective based on the existence  
 384 of a critical point,  $\xi(\mathbf{p}_{crit.})$ , associated with the SF (SM, S9). A crucial re-  
 385 sult that motivated us to adopt such an approach is that pain-related mutation  
 386 sites are attracted toward the critical point in sheer contrast to neutral mutation  
 387 sites which are repelled from it (Figure 5(b)). We term this phenomenon critical  
 388 clustering. Geometrically, the formation of the critical mutation sites cluster re-  
 389 flects the tendency of structural locations of pain-related mutations to minimize  
 390 their distance from the surface of the critical sphere of radius  $\xi(\mathbf{p}_{crit.}) \approx 33.4$   
 391 Å; intuitive graphical representation of this phenomenon is provided in Figure  
 392 5(a) where we show that "hot" areas I and II intersect with the dashed green  
 393 line  $\xi(\mathbf{p}_{crit.})$  representing critical sphere's surface (Figure 5(a)).

394 Armed with the observation that pain-related mutation sites (in contrast to  
 395 neutrals) tend to occupy locations at critical hydrophobic-interactions distance  
 396 from the SF, we focused on the scaling behavior of HIIS around the critical  
 397 point that is adequately described in terms of the power-law scheme

$$m_z^{(1)}(\mathbf{p}_{crit.}, l_\alpha(\mathbf{p}_{crit.})) \sim \begin{cases} l_\alpha(\mathbf{p}_{crit.})^{\gamma_{partI}(\mathbf{p}_{crit.})} & \text{for } s(\mathbf{p}_{crit.}) < l_\alpha(\mathbf{p}_{crit.}) \leq \xi(\mathbf{p}_{crit.}) \\ l_\alpha(\mathbf{p}_{crit.})^{\gamma_{partII}(\mathbf{p}_{crit.})} & \text{for } \xi(\mathbf{p}_{crit.}) < l_\alpha(\mathbf{p}_{crit.}) \leq o(\mathbf{p}_{crit.}) \end{cases} \quad (r1)$$

398 accounting for a HIs-network expansion and contraction within the pre- and  
 399 post-inflection phase intervals  $s(\mathbf{p}_{crit.}) < l_\alpha(\mathbf{p}_{crit.}) \leq \xi(\mathbf{p}_{crit.})$  and  $\xi(\mathbf{p}_{crit.}) <$   
 400  $l_\alpha(\mathbf{p}_{crit.}) \leq o(\mathbf{p}_{crit.})$  with rates of  $\gamma_{partI}(\mathbf{p}_{crit.}) = 2.27 \pm 0.18$  and  $\gamma_{partII}(\mathbf{p}_{crit.}) =$   
 401  $-5.18 \pm 1.02$ , respectively (Figure 5(c)). On the left of the interval  $\xi(\mathbf{p}_{crit.}) <$   
 402  $l_\alpha(\mathbf{p}_{crit.}) \leq \nu(\mathbf{p}_{crit.})$ , both, the range and intensity of HIIS maximize as the  
 403 HIs-network configuration exceeds its critical size marking the transition from  
 404 the pre-inflection phase toward the post-inflection phase. The energy levels

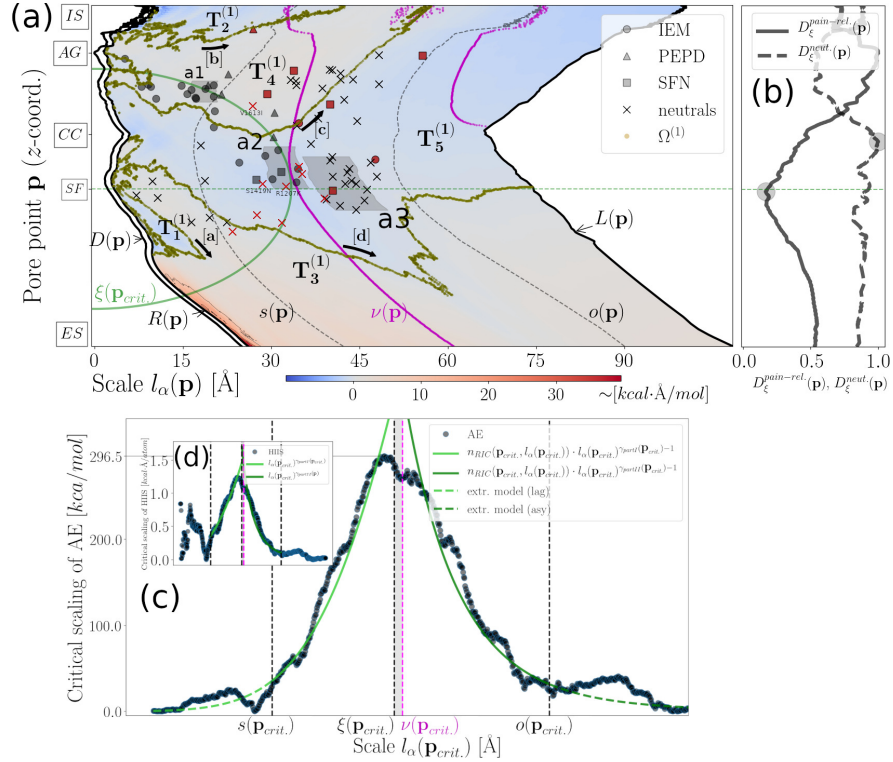
405 associated with this phase transition are given by

$$U(\mathbf{p}_{crit.}, l_\alpha(\mathbf{p}_{crit.})) \sim \begin{cases} N(\mathbf{p}_{crit.}, l_\alpha(\mathbf{p}_{crit.})) \cdot l_\alpha(\mathbf{p}_{crit.})^{\gamma_{partI}(\mathbf{p}_{crit.})-1} & \text{for } s(\mathbf{p}_{crit.}) < l_\alpha(\mathbf{p}_{crit.}) \leq \xi(\mathbf{p}_{crit.}) \\ N(\mathbf{p}_{crit.}, l_\alpha(\mathbf{p}_{crit.})) \cdot l_\alpha(\mathbf{p}_{crit.})^{\gamma_{partII}(\mathbf{p}_{crit.})-1} & \text{for } \xi(\mathbf{p}_{crit.}) < l_\alpha(\mathbf{p}_{crit.}) \leq o(\mathbf{p}_{crit.}) \end{cases} \quad (\text{r2})$$

406 where  $N(\mathbf{p}_{crit.}, l_\alpha(\mathbf{p}_{crit.}))$  can be replaced with its best-fitted Richards model,  
 407  $n_{ric}(\mathbf{p}_{crit.}, l_\alpha(\mathbf{p}_{crit.}))$  (see caption of Figure 5 for Richards model parameters),  
 408 providing with an estimation of the atom-packing energy (AE) (Figure 5(c)).  
 409 Similarly to the NaVAb case [66], AE maximization occurs in the vicinity of the  
 410 interval  $\xi(\mathbf{p}_{crit.}) < l_\alpha(\mathbf{p}_{crit.}) \leq \nu(\mathbf{p}_{crit.})$  so that energetic coupling of the PMs  
 411 with the VSs is dictated by the phase transition (Figure 5(c),(d)).

412 Equation r1 indicates that inter-atomic HIs law is robust to microscopic  
 413 modifications of the atomic structure, e.g., addition, removal or deletion of  
 414 a small number of atoms corresponding to small-amplitude perturbations of  
 415  $N(\mathbf{p}_{crit.}, l_\alpha(\mathbf{p}_{crit.}))$  [85]. This happens however at the cost of re-tuning HI-  
 416 cIS and, hence, also of AE that, in the case of small-amplitude perturbations  
 417 of  $N(\mathbf{p}_{crit.}, l_\alpha(\mathbf{p}_{crit.}))$ , are expected to be up- and down-regulated toward and  
 418 away from the critical point, respectively, in a power-law fashion described by  
 419 r2 (Figure 5(c)). Mutation-induced perturbations propagating throughout the  
 420 structure are thus expected to be amplified in the vicinity of the critical point  
 421 while, on the other hand, to be damped out toward the interior (i.e., toward  
 422 the HP and the SF) and toward channel exterior bounded by outer pore surface  
 423 radius. Given that mutations in the structural proximity of the SF are highly  
 424 likely to have a deleterious LOF effect [86], observed damping-out mechanism  
 425 might act as a shield protecting SF's biological machinery from mutations occur-  
 426 ring within the pre-inflection phase. On the other hand, mutations occurring in  
 427 the post-inflection phase are unlikely to affect the SF as they have to overcome  
 428 a large energy barrier in order to reach channel interior. We thus hypothesize  
 429 that critical clustering of pain-related mutations might actually reflect a trade-  
 430 off between the two extremes; a destructive destabilization and an insignificant  
 431 one.

432



433

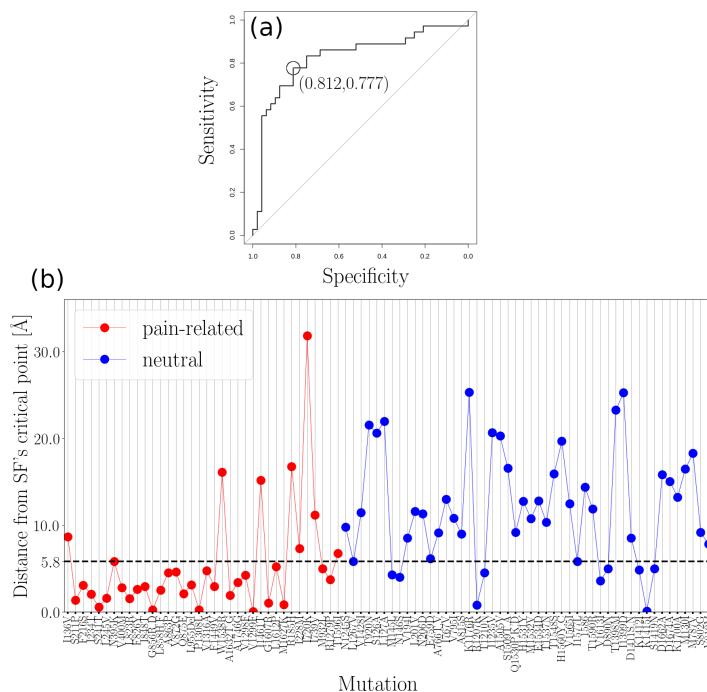
434 **Figure 5: Spatial profile of HIIS along NaV1.7's pore.** (a), Contour map of  
 435 HIIS axial part,  $m_z^{(1)}(\mathbf{p}, l_\alpha(\mathbf{p}))$ , for  $\mathbf{p} \in P$  and  $\alpha = 1, 2, \dots, K_\alpha = 800$ . Blue and  
 436 red color contour domains represent configurations of  $\tilde{\mathbf{m}}_z^{(1)}(\mathbf{p}, l_\alpha(\mathbf{p}))$  with  
 437 orientation "out" and "in", respectively. Black lines  $R(\mathbf{p})$ ,  $\bar{R}(\mathbf{p})$  and  $L(\mathbf{p})$  depict  
 438 geometrical pore characteristics. Magenta dashed line  $\nu(\mathbf{p})$  represents the PMS-VSs  
 439 spatial transition. Dashed black lines  $s(\mathbf{p})$ ,  $\xi(\mathbf{p})$  and  $o(\mathbf{p})$  account for the bound-  
 440 aries between different domains.  $\xi(\mathbf{p}_{crit.})$  represents the critical radius. Black arrows  
 441 [a], [b], [c], [d] and [e] indicate the clustering behavior of the zero-crossing points of  
 442  $m_z^{(1)}(\mathbf{p}, l_\alpha(\mathbf{p}))$  collected in  $\Omega^{(1)}$  describing boundaries among contour domains  $T_1^{(1)}$ ,  
 443  $T_2^{(1)}$ ,  $T_3^{(1)}$ ,  $T_4^{(1)}$  and  $T_5^{(1)}$ . Mutations sites highlighted with red color correspond to  
 444 misclassified events. Grey-shaded areas "a1", "a2" and "a3" highlight map areas where  
 445 map density of mutation sites maximizes. (b), Distance between inflection points and  
 446 mutation sites along the pore is also plotted in terms of the normalized (with respect  
 447 to maximum value) statistical representations  $\bar{D}_\xi^{path.}(\mathbf{p})$  and  $\bar{D}_\xi^{cont.}(\mathbf{p})$ , respectively.  
 448 (c), Power-law scaling of HIIS axial part for  $\mathbf{p}_{crit.} = (p_x \approx 0, p_y \approx 0, p_z = -12.1)$ .  
 449 The best-fitting first-part-inflection-domain and second-part-inflection-domain power-  
 450 law approximations are also plotted with mean absolute relative fitting errors being  
 451  $0.09 \pm 0.01$  and  $0.15 \pm 0.03$ , respectively. (d), Power-law-like behavior of AE,  $U(\mathbf{p}, l_\alpha(\mathbf{p}))$   
 452 for  $\mathbf{p}_{crit.} = (p_x \approx 0, p_y \approx 0, p_z = -12.1)$ . First- and second-part-inflection-domain  
 453 modeling approximations of AE are also plotted with their mean absolute relative modeling  
 454 errors being  $0.11 \pm 0.02$  and  $0.14 \pm 0.03$ , respectively. AE model extrapolation toward the

455 lag-domain  $l_\alpha(\mathbf{p}) \leq s(\mathbf{p})$  and the asymptote-domain  $l_\alpha(\mathbf{p}) > o(\mathbf{p})$  result in a mean ab-  
456 solute relative fitting error of  $6.06 \pm 16.0$  and  $1.55 \pm 6.39$ , respectively. Richards model  
457 parameters used for modeling AE are  $\{A(\mathbf{p}_{crit.}) = 1.03, t(\mathbf{p}_{crit.}) = 0.03, s(\mathbf{p}_{crit.}) =$   
458  $18.16, \tilde{q}(\mathbf{p}_{crit.}) = 0.47\}$ .

459

460 We tested the critical-clustering hypothesis by calculating the distance each  
461 mutation structural location and SF's critical point (SM, S8), and feeding re-  
462 trieved distances into a binary classifier. We achieved to classify correctly 28  
463 (out of 36) and 39 (out of 48) of pain-related and neutral mutations correctly  
464 with a cut-off distance of 5.8 Å. This translates to an area under receiver oper-  
465 ating characteristics (ROC) curve of 0.824 and pain phenotype prediction with  
466 specificity of 0.812 and sensitivity of 0.777 (Figure 6(a)). Intuitive geometri-  
467 cal depiction of this result requires to think of a "hot" spherical shell squeezed  
468 between the spheres of radii  $\xi(\mathbf{p}_{crit.}) + 5.8$  Å and  $\xi(\mathbf{p}_{crit.}) - 5.8$  Å centered at  
469  $\mathbf{p}_{crit.}$  incorporating areas I and II thus containing the majority of pain-related  
470 structural locations. This tendency can be deduced from Figure 5 where we  
471 can see that correctly-classified pain-related and neutral sites tend to minimize  
472 and maximize, respectively, their distance from the critical radius  $\xi(\mathbf{p}_{crit.})$ . The  
473 opposite holds for misclassified mutations. Note however that due to the pore  
474 points offset, distances of sites from  $\xi(\mathbf{p}_{crit.})$  line on Figure 5 are not equal with  
475 the distances of their structural locations from the surface of the sphere of  $\xi(\mathbf{p})$   
476 (discrepancies are of order  $\approx 3.13 \pm 4.63$  Å). Misclassified pain-related mutations  
477 are I136V, W1538R, I1461T, R185H, I228M, I720K, I739V and T1596I indicat-  
478 ing that sensitivity output is qualitatively similar to the HP-based classification  
479 attempt. On the other hand, quality of specificity differs significantly among  
480 classification attempts as critical-point distance criterion misclassified neutrals  
481 M145L, M146S, R1207K, T1210N, V1613I, D890N, K1412I, K1415I and S1419N  
482 are clustering within the "hot" spherical shell in proximity to HP's boundary.

483



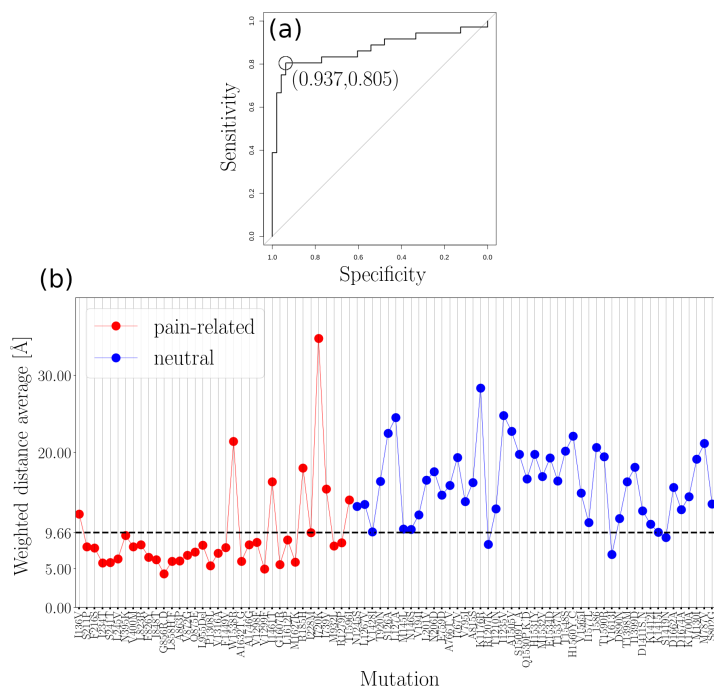
484

485 *Figure 6: Binary classification of NaV1.7 variants based on their distance*  
 486 *from SF's critical point. (a), ROC curve constructed based on SF's-critical-point*  
 487 *distance data (for construction of data set see SM, S8). Optimal threshold value 5.8*  
 488 *Å corresponds to specificity and sensitivity values of 0.812 and 0.777, respectively. Area*  
 489 *under ROC curve is 0.824. (b), Visualization of ROC curve data. Optimal threshold*  
 490 *value 5.8 Å is marked with black dashed line. ROC curve is constructed in R [67] by*  
 491 *using the pROC package [84].*

492

493 Finally, in order to harvest the classification power of both predictors, we  
 494 linearly combined distance metrics by calculating a weighted distance average  
 495 (SM, S10). The weighted distance average achieved to classify correctly 29 (out  
 496 of 36) pain-related mutations and 45 (out of 48) neutrals, i.e., sensitivity =  
 497 0.805, specificity = 0.937, area under ROC curve = 0.872 (Figure 7(a)). The  
 498 threshold weighted distance value is 9.6 Å and it indicates which mutations are  
 499 found in proximity to SF's critical point and HP's boundary.

500



501

502 **Figure 7: Binary classification of NaV1.7 variants based on the weighted distance**  
 503 **average.** (a), ROC curve constructed based on weighted distance data (for  
 504 construction of data set see SM, S8). Optimal threshold value 9.6 Å corresponds to  
 505 specificity and sensitivity values of 0.805 and 0.937, respectively. Area under ROC  
 506 curve is 0.872. (b), Visualization of ROC curve data. Optimal threshold value 9.6 Å is  
 507 marked with black dashed line. ROC curve is constructed in R [67] by using the pROC  
 508 package [84].

509

510 The relatively-low sensitivity of the weighted distance average is not surpris-  
 511 ing if we consider that both classifications attempts failed in correctly classifying  
 512 pain-related mutations found far away from the HP and from the SF; misclassi-  
 513 fied pain-related mutations are I136V, W1538R, I1461T, R185H, I720K, I739V  
 514 and T1596I and all of them are found within the post-inflection phase with the  
 515 exception of I1461T which is located within the lag domain but still far away  
 516 from the HP and from the SF (Figure 3, 5(a) and 7). On the other hand, mis-  
 517 classified neutrals R1207K, V1613I and S1419N occupy "hot" spots located in  
 518 proximity to SF's critical point and HP's boundary (Figure 3, 5(a) and 7).

## 519 Discussion and concluding remarks

520 Criticality hypothesis in biology aims at explaining how emergence of power-  
 521 laws increases biological system's robustness and efficiency hand-in-hand with  
 522 evolution. Empirical evidence for complex biological systems operating near  
 523 critical points include cases of gene expression [87], DNA sequences [88], protein

524 structures [60, 61, 62, 63], cell growth [89] and neuronal dynamics underlying  
525 brain activity [90]. In practice, criticality implies that system dynamics are  
526 delicately balanced between an ordered state where perturbations are damped-  
527 out and a disordered state where perturbations are amplified. Consequences  
528 of critical dynamics are associated with optimal information processing [91],  
529 enhanced network stability [92] and maximal sensitivity to external stimuli [93].

530 In this work, instead of trying to predict the effect of missense *SCN9A*-  
531 gene mutations via comparing mutant NaV1.7 structures *in silico*, we extracted  
532 hydrophobic features of the wild-type atomic environment encoding NaV1.7's  
533 response to mutation-induced variations. Stated differently, we hypothesized  
534 that some regions of the atomic environment around NaV1.7's pore exhibit  
535 higher sensitivity to mutation-induced perturbations due to the long-range na-  
536 ture of HIs guaranteeing their stability; a hallmark of SOC is that avalanche-like  
537 perturbing effects are amplified and fast-spreading throughout critical network  
538 locations [94]. To test this hypothesis we mapped mutation structural locations  
539 on their corresponding mutation sites and probed topological and scaling hydro-  
540 pathic characteristics of the atomic bulk around the pore. Importantly, this is  
541 possible due to the relatively-large number of pain-related mutations providing  
542 with the opportunity of structure-based mutation statistics and, consequently,  
543 identification of densely-populated (by mutation sites) structural domains.

544 The starting point of the presented procedures was the approximation of the  
545 atomic cumulative distribution function around NaV1.7's pore demonstrating  
546 that packing of atoms follows a sigmoid accumulation pattern. The generality of  
547 the Richards model was found to be adequate for this modeling purpose verifying  
548 the sigmoid accumulation hypothesis and, consequently, revealing a biphasic  
549 spatial organization of the atomic environment around the pore dictated by  
550 the spatial transition from the PM from the VSs. We showed that the pore is  
551 lined by a HP dominating within channel interior and that HIs stabilizing atom-  
552 packing around the SF are critically tuned with respect to the local inflection  
553 points. This NaV1.7 feature is shared with its evolutionary-ancestor, namely,  
554 with the pre-open NaVA channel, suggesting that HIs scale-invariance might  
555 be conserved from NaVChs of bacterial homomers to NaVChs of mammalian  
556 heteromers [66].

557 Pain-related mutations tend to occupy structural locations in proximity to  
558 the HP while maintaining a critical HIs-distance from the SF. Geometrically, this  
559 result indicates that the majority of pain-related mutations are found within a  
560 spherical shell around the SF incorporating parts of the HP. What might be the  
561 evolutionary principle underlying this non-random mutation distribution around  
562 NaV1.7's pore? Given that the DEKA SF sequence is conserved among human  
563 and non-human NaVCh templates [95], we propose that expression of mutations  
564 at critical hydrophobic-interactions distance from the SF might reflect an evolu-  
565 tionary trade-off between potentially-deleterious destabilizations occurring too  
566 close to the SF and insignificant polymorphisms occurring far away from it. Ac-  
567 cording to this rationale, mutations occupying critical hydrophobic-interactions  
568 network locations lead to a GOF effect by increasing channel's configuration  
569 space and, consequently, expanding physiological range of ionic currents, while

570 not risking structure deletion or severe destabilizations that can induce a LOF  
571 effect [86].

572 Misclassification of seven pain-related events found within the post-inflection  
573 phase (namely, of I136V, W1538R, I1461T, R185H, I720K, I739V and T1596I)  
574 suggests that the destabilizing mutation effect within the post-inflection phase  
575 and, specifically, within the VSs needs to be locally investigated. In particular,  
576 misclassified pain-related events are likely to affect local properties of the VSs  
577 which are however crucial for physiological gating and ionic currents. It might  
578 therefore be useful for future studies to consider a decoupling of the PM from  
579 the VSs in order to focus solely on the cumulative hydrophobic topology and  
580 HIs-networking within the VSs. Moreover, a goal for follow-up studies is to  
581 include biophysical characteristics of substituted amino acids (e.g., size, charge,  
582 hydrophobicity-property, degree of conservation) into our model as this might  
583 not only improve classification accuracy but also provide with a more detailed  
584 picture of the mutation effect.

585 Admittedly, a limitation of this study is the small (from a statistics point  
586 of view) number of available mutation events. To resolve this issue and pro-  
587 vide with stronger statistical validation, we may consider in future studies to  
588 increase number of neutral and pain-related mutations, for example, by intro-  
589 ducing NaV1.7 variants found in the Genome Aggregation Database (gnomAD)  
590 [96]. A methodological weakness is that we neglected radial hydrophobic ef-  
591 fects. In particular, even if the amplitude of the radial HHS component is small  
592 in comparison to the amplitude of the axial HHS component, its role might  
593 be non-negligible for interactions between ions and pore walls. Moreover, it is  
594 important to remind at this point that we chose to work with a closed-state  
595 structural model of the NaV1.7 which most likely corresponds to a pre-open  
596 state of NaV1.7's gating cycle. The rationale underlying this choice was that  
597 we sought to establish a connection (if any) between the closed-state NaV1.7  
598 and the closed-state NaVA before we focus on the human NaV1.7 structure  
599 captured at an inactivated state [95].

600 Our findings suggest that pathogenicity of NaV1.7 variants can be predicted  
601 if corresponding mutation structural locations are in structural and, hence, also  
602 hydrophobic proximity to either the HP or the SF. Prediction of pathogenicity  
603 can then be performed with negligible computational effort and similar or even  
604 higher accuracy to [56] (reported accuracy: 0.81) but also to the more recent  
605 study of [97] where a MLE computational pipeline was employed (reported ac-  
606 curacy on the human NaV1.7 template: 63.5%). In an era where MLE pipelines  
607 become increasingly popular, the phenomenological framework curated in this  
608 study could provide biophysical rationalization to MLE-retrieved predictions for  
609 NaVCh pathophysiological characterization; crucially, hydrophobicity-property  
610 is recognized as a key-feature for predicting functional effects of genetic defects  
611 in NaVChs, as well as, in voltage-gated calcium channels [86].

612 **Declarations**

613 *Ethics approval and consent to participate*

614 Not applicable.

615 *Consent for publication*

616 Not applicable.

617 *Availability of data and materials*

618 Data sharing is not applicable to this article as no datasets were generated  
619 or analyzed during the current study. The 3D structural model of the NaV1.7  
620 channel is available from the authors with permission of YY and SGW.

621 *Competing interests*

622 The authors declare that they have no competing interests.

623 *Funding*

624 The study was partly funded by the European Union 7th Framework Pro-  
625 gramme (grant n602273).

626 *Authors' contributions*

627 MNX designed the study, performed computations and data analysis. RW  
628 and PL contributed to refinement of algorithmic steps. YY provided with the 3D  
629 structural model of the NaV1.7 channel, MMG contributed to variants selection  
630 and analysis, RW, PL, DK, YY, JH, HJS and SGW provided with critical feed-  
631 back and helped with the interpretation of the results; YY and SGW encouraged  
632 MNX to focus on specific aspects of the findings. HJS supervised the study. GL  
633 and CGF were in charge of overall direction. MNX wrote the manuscript in  
634 consultation with all the co-authors. All co-authors have critically revised the  
635 manuscript.

636 *Acknowledgments*

637 We acknowledge technical and scientific support provided by the PROPANE  
638 study group.

639 **References**

- 640 [1] Cheng, X., Dib-Hajj, S.D., Tyrrell, L., Waxman, S.G. Mutation I136V alters  
641 electrophysiological properties of the Na(v)1.7 channel in a family with onset  
642 of erythromelalgia in the second decade. *Mol Pain* **4**, 1 (2008).
- 643 [2] Estacion, M., Choi, J.S., Eastman, E.M. et al. Can robots patch-clamp as  
644 well as humans? Characterization of a novel sodium channel mutation. *J*  
645 *Physiol* **588**, 1915-1927 (2010).
- 646 [3] Wu, M.T., Huang, P.Y., Yen, C.T., Chen, C.C., Lee, M.J. A novel SCN9A  
647 mutation responsible for primary erythromelalgia and is resistant to the  
648 treatment of sodium channel blockers. *PLoS One* **8**, e55212 (2013).
- 649 [4] Choi, J.S., Dib-Hajj, S.D., Waxman, S.G. Inherited erythromelalgia: limb  
650 pain from an S4 charge-neutral Na channelopathy. *Neurology* **67**, 1563-1567  
651 (2006).
- 652 [5] Ahn, H.S., Dib-Hajj, S.D., Cox, J.J. et al. A new Nav1.7 sodium channel  
653 mutation I234T in a child with severe pain. *Eur J Pain* **14**, 944-950 (2010).
- 654 [6] Lampert, A., Dib-Hajj, S.D., Tyrrell, L., Waxman, S.G. Size matters: Ery-  
655 thromelalgia mutation S241T in Nav1.7 alters channel gating. *J Biol Chem*  
656 **281**, 36029-36035 (2006).
- 657 [7] Yang, Y., Dib-Hajj, S.D., Zhang, J. et al. Structural modelling and mutant  
658 cycle analysis predict pharmacoresponsiveness of a Na(V)1.7 mutant chan-  
659 nel. *Nat Commun* **3**, 1186 (2012).
- 660 [8] Emery, E.C., Habib, A.M., Cox, J.J. et al. Novel SCN9A mutations under-  
661 lying extreme pain phenotypes: unexpected electrophysiological and clinical  
662 phenotype correlations. *J Neurosci* **35**, 7674-7681 (2015).
- 663 [9] Sheets, P.L., Jackson, J.O. 2nd, Waxman, S.G., Dib-Hajj, S.D., Cummins,  
664 T.R. A Nav1.7 channel mutation associated with hereditary erythromelal-  
665 gia contributes to neuronal hyperexcitability and displays reduced lidocaine  
666 sensitivity. *J Physiol* **581**, 1019-1031 (2007).
- 667 [10] Fischer, T.Z., Gilmore, E.S., Estacion, M. et al. A novel Nav1.7 mutation  
668 producing carbamazepine-responsive erythromelalgia. *Ann Neurol* **65**, 733-  
669 741 (2009).
- 670 [11] Lampert, A., Dib-Hajj, S.D., Eastman, E.M., Tyrrell, L., Lin, Z., Yang, Y.,  
671 Waxman, S.G. Erythromelalgia mutation L823R shifts activation and inac-  
672 tivation of threshold sodium channel Nav1.7 to hyperpolarized potentials.  
673 *Biochem Biophys Res Commun* **390**, 319-324 (2006)..
- 674 [12] Wu, B., Zhang, Y., Tang, H. et al. A Novel SCN9A Mutation (F826Y) in  
675 Primary Erythromelalgia Alters the Excitability of Nav1.7. *Curr Mol Med*  
676 **17**, 450-457 (2017).

- 677 [13] Cummins, T.R., Dib-Hajj, S.D., Waxman, S.G. Electrophysiological prop-  
678 erties of mutant Nav1.7 sodium channels in a painful inherited neuropathy.  
679 *J Neurosci* **24**, 8232-8236 (2004).
- 680 [14] Han, C., Dib-Hajj, S.D., Lin, Z. et al. Early- and late-onset inherited ery-  
681 thromelalgia: genotype-phenotype correlation. *Brain* **132**, 1711-1722 (2009).
- 682 [15] Theile, J.W., Cummins, T.R. Inhibition of Nav $\beta$ 4 peptide-mediated resur-  
683 gent sodium currents in Nav1.7 channels by carbamazepine, riluzole, and  
684 anandamide. *Mol Pharmacol* **80**, 724-734 (2011).
- 685 [16] Tanaka, B.S., Nguyen, P.T., Zhou, E.Y. et al. Gain-of-function mutation  
686 of a voltage-gated sodium channel Nav1.7 associated with peripheral pain  
687 and impaired limb development. *J Biol Chem* **292**, 9262-9272 (2017).
- 688 [17] Hoeijmakers, J.G., Han, C., Merkies, I.S. et al. Small nerve fibres, small  
689 hands and small feet: a new syndrome of pain, dysautonomia and acrome-  
690 somelia in a kindred with a novel Nav1.7 mutation. *Brain* **135**, 345-358  
691 (2012).
- 692 [18] Cummins, T.R., Dib-Hajj, S.D., Waxman, S.G. Electrophysiological prop-  
693 erties of mutant Nav1.7 sodium channels in a painful inherited neuropathy.  
694 *J. Neurosci* **24**, 8232-8236 (2004).
- 695 [19] Rush, A.M., Dib-Hajj, S.D., Liu, S., Cummins, T.R., Black, J.A., Waxman,  
696 S.G. A single sodium channel mutation produces hyper- or hypoexcitability  
697 in different types of neurons. *Proc Nat Acad Sci USA* **103**, 8245-8250 (2006).
- 698 [20] Han, C., Rush, A.M., Dib-Hajj, S.D. et al. Sporadic onset of erythromelgia:  
699 a gain-of-function mutation in Nav1.7. *Ann Neurol* **59**, 553-558 (2006).
- 700 [21] Harty, T.P., Dib-Hajj, S.D., Tyrrell, L., Blackman, R., Hisama, F.M., Rose,  
701 J.B., Waxman, S.G. Nav1.7 mutant A863P in erythromelgia: effects of  
702 altered activation and steady-state inactivation on excitability of nociceptive  
703 dorsal root ganglion neurons. *J Neurosci* **26**, 12566-12575 (2006).
- 704 [22] Choi, J.S., Zhang, L., Dib-Hajj, S.D. et al. Mexiletine-responsive ery-  
705 thromelalgia due to a new Nav1.7 mutation showing use-dependent current  
706 fall-off. *Exp Neurol* **216**, 383-389 (2009).
- 707 [23] Stadler, T., O'Reilly, A.O., Lampert, A. Erythromelgia mutation Q875E  
708 Stabilizes the activated state of sodium channel Nav1.7. *J Biol Chem* **290**,  
709 6316-6325 (2015).
- 710 [24] Cheng, X., Dib-Hajj, S.D., Tyrrell, L., Te Morsche, R.H., Drenth, J.P.,  
711 Waxman, S.G. Deletion mutation of sodium channel Nav1.7 in inherited  
712 erythromelgia: enhanced slow inactivation modulates dorsal root ganglion  
713 neuron hyperexcitability. *Brain* **134**, 1972-1986 (2011).

- 714 [25] Cheng, X., Dib-Hajj, S.D., Tyrrell, L., Wright, D.A., Fischer, T.Z., Wax-  
715 man, S.G. Mutations at opposite ends of the DIII/S4-S5 linker of sodium  
716 channel Nav1.7 produce distinct pain disorders. *Mol Pain* **6**, 24 (2010).
- 717 [26] Estacion, M., Yang, Y., Dib-Hajj, S.D. et al. A new Nav1.7 mutation in an  
718 erythromelalgia patient. *Biochem Biophys Res Commun* **432**, 99-104 (2013).
- 719 [27] Wu, M.T., Huang, P.Y., Yen, C.T., Chen, C.C., Lee, M.J. A novel SCN9A  
720 mutation responsible for primary erythromelalgia and is resistant to the  
721 treatment of sodium channel blockers. *PLoS One* **8**, e55212 (2013).
- 722 [28] Dib-Hajj, S.D., Rush, A.M., Cummins, T.R. et al. Gain-of-function muta-  
723 tion in Nav1.7 in familial erythromelalgia induces bursting of sensory neu-  
724 rons. *Brain* **128**, 1847-1854 (2005).
- 725 [29] Cregg, R., Laguda, B., Werdehausen, R. et al. Novel mutations mapping  
726 to the fourth sodium channel domain of Nav1.7 result in variable clinical  
727 manifestations of primary erythromelalgia. *Neuromolecular Med* **15**, 265-  
728 278 (2013).
- 729 [30] Eberhardt, M., Nakajima, J., Klinger, A.B. et al. Inherited pain: sodium  
730 channel Nav1.7 A1632T mutation causes erythromelalgia due to a shift of  
731 fast inactivation. *J Biol Chem* **289**, 1971-1980 (2014).
- 732 [31] Yang, Y., Huang, J., Mis, M.A. et al. Nav1.7-A1632G Mutation from a  
733 Family with Inherited Erythromelalgia: Enhanced Firing of Dorsal Root  
734 Ganglia Neurons Evoked by Thermal Stimuli. *J Neurosci* **36**, 7511-7522  
735 (2016).
- 736 [32] Jarecki, B.W., Sheets, P.L., Jackson, J.O. 2nd, Cummins, T.R. Paroxys-  
737 mal extreme pain disorder mutations within the D3/S4-S5 linker of Nav1.7  
738 cause moderate destabilization of fast inactivation. *J Physiol* **586**, 4137-4153  
739 (2008).
- 740 [33] Jarecki, B.W., Sheets, P.L., Jackson, J.O. 2nd, Cummins, T.R. Paroxys-  
741 mal extreme pain disorder mutations within the D3/S4-S5 linker of Nav1.7  
742 cause moderate destabilization of fast inactivation. *J Physiol* **586**, 4137-4153  
743 (2008).
- 744 [34] Theile, J.W., Jarecki, B.W., Piekarz, A.D., Cummins, T.R. Nav1.7 muta-  
745 tions associated with paroxysmal extreme pain disorder, but not erythrome-  
746 lalgia, enhance Nav $\beta$ 4 peptide-mediated resurgent sodium currents. *J Phys-  
747 iol* **589**, 597-608 (2011).
- 748 [35] Fertleman, C.R., Baker, M.D., Parker, K.A. et al. SCN9A mutations in  
749 paroxysmal extreme pain disorder: allelic variants underlie distinct channel  
750 defects and phenotypes. *Neuron* **52**, 767-774 (2006).

- 751 [36] Choi, J.S., Boralevi, F., Brissaud, O. et al. Paroxysmal extreme pain disorder: a molecular lesion of peripheral neurons. *Nat Rev Neurol* **7**, 51-55  
752 (2011).  
753
- 754 [37] Suter, M.R., Bhuiyan, Z.A., Laedermann, C.J. et al. p.L1612P, a novel  
755 voltage-gated sodium channel Nav1.7 mutation inducing a cold sensitive  
756 paroxysmal extreme pain disorder. *Anesthesiology* **122**, 414-423 (2015).
- 757 [38] Dib-Hajj, S.D., Estacion, M., Jarecki, B.W. et al. Paroxysmal extreme  
758 pain disorder M1627K mutation in human Nav1.7 renders DRG neurons  
759 hyperexcitable. *Mol Pain* **4**, 37 (2008).
- 760 [39] Estacion, M., Dib-Hajj, S.D., Benke, P.J. et al. NaV1.7 gain-of-function  
761 mutations as a continuum: A1632E displays physiological changes associated  
762 with erythromelalgia and paroxysmal extreme pain disorder mutations and  
763 produces symptoms of both disorders. *J Neurosci* **28**, 1079-11088 (2008).
- 764 [40] Han, C., Hoeijmakers, J.G., Liu, S. et al. Functional profiles of SCN9A  
765 variants in dorsal root ganglion neurons and superior cervical ganglion neurons  
766 correlate with autonomic symptoms in small fibre neuropathy. *Brain*  
767 **135**, 2613-2628 (2012).
- 768 [41] Estacion, M., Han, C., Choi, J.S. et al. Intra- and interfamily phenotypic  
769 diversity in pain syndromes associated with a gain-of-function variant of  
770 NaV1.7. *Mol Pain* **7**, 92 (2011).
- 771 [42] Faber, C.G., Hoeijmakers, J.G., Ahn, H.S. et al. Gain of function Nav1.7  
772 mutations in idiopathic small fiber neuropathy. *Ann. Neurol.* **71**, 26-39  
773 (2012).
- 774 [43] Huang, J., Yang, Y., Dib-Hajj, S.D. et al. Depolarized inactivation over-  
775 comes impaired activation to produce DRG neuron hyperexcitability in a  
776 Nav1.7 mutation in a patient with distal limb pain. *J Neurosci* **34**, 12328-  
777 12340 (2014).
- 778 [44] Blesneac, I., Themistocleous, A.C., Fratter, C. et al. Rare NaV1.7 variants  
779 associated with painful diabetic peripheral neuropathy. *Pain* **159**, 469-480  
780 (2018).
- 781 [45] Cox J.J., Reimann, F., Nicholas, A.K. et al. An SCN9A channelopathy  
782 causes congenital inability to experience pain. *Nature* **444**, 894-898 (2006).
- 783 [46] Goldberg, Y.P., MacFarlane, J., MacDonald, M.L. et al. Loss-of-function  
784 mutations in the NaV1.7 gene underlie congenital indifference to pain in  
785 multiple human populations. *Clin Genet* **71**, 311-319 (2007).
- 786 [47] Nilsen, K.B., Nicholas, A.K., Woods, C.G., Mellgren, S.I., Nebuchennykh,  
787 M., Aasly, J. Two novel SCN9A mutations causing insensitivity to pain.  
788 *Pain* **143**, 155-158 (2009).

- 789 [48] Hammer, M.U., Anderson, T.H., Chaimovich, A., Shell, M.S., Israelachvili,  
790 J. The search for the hydrophobic force law. *Faraday Discuss* **146**, 299-308  
791 (2010).
- 792 [49] Hummer, G., Garde, S., García, A.E., Paulaitis, M.E., Pratt, L.R. Hy-  
793 drophobic Effects on a Molecular Scale. *J Phys Chem B* **102**, 51 (1998).
- 794 [50] Aryal, P., Sansom M.S.P, Tucker, S.J. Hydrophobic Gating in Ion Channels.  
795 *J Mol Biol* **427**, 121-130 (2015).
- 796 [51] Li, E., Wimley, W.C., Hristova, K. Transmembrane helix dimeriza-  
797 tion:beyond the search for sequence motifs. *Biochim Biophys Acta* **1818**,  
798 183-193 (2012).
- 799 [52] Lin, J., Motylinski, J., Krauson, A. J., Wimley, W. C., Searson, P.C.,  
800 Hristova, K. Interactions of membrane active peptides with planar supported  
801 bilayers: an impedance spectroscopy study. *Langmuir* **28**, 6088-6096 (2012).
- 802 [53] Yonkunas, M., Kurnikova, M. The hydrophobic effect contributes to the  
803 closed state of a simplified ion channel through a conserved hydrophobic  
804 patch at the pore-helix crossing. *Front Pharmacol* **6**, 284 (2015).
- 805 [54] Lampert, A., O'Reilly, A.O., Dib-Hajj, S.D., Tyrrell, L., Wallace, B.A.,  
806 Waxman, S.G. A Pore-blocking Hydrophobic Motif at the Cytoplasmic  
807 Aperture of the Closed-state Nav1.7 Channel Is Disrupted by the  
808 Erythromelalgia-associated F1449V Mutation. *J Biol Chem* **283**, 24118-  
809 24127 (2008).
- 810 [55] Yang, Y., Estacion, M., Dib-Hajj, S.D., Waxman, S.G. Molecular Archi-  
811 tecture of a Sodium Channel S6 Helix: radial tuning of the voltage-gated  
812 sodium channel 1.7 activation gate. *J Biol Chem* **288**, 13741-13747 (2013).
- 813 [56] Kapetis, D., Yang, Y., Sassone, J. et al. Network topology of Nav1.7 mu-  
814 tations in sodium channel-related painful disorders. *BMC Systems Biology*  
815 **11**, 28 (2017).
- 816 [57] Hasan S., Hunter T., Hunter G., Pessia M., D'Adamo M.C. Commentary:  
817 A channelopathy mutation in the voltage-sensor discloses contributions of a  
818 conserved phenylalanine to gating properties of Kv1.1 channels and ataxia.  
819 *Front Cell Neurosci* **12**, 174 (2018).
- 820 [58] Payandeh, J., Scheuer, T., Zheng, N., Catterall, W.A. The crystal structure  
821 of a voltage-gated sodium channel. *Nat* **475**, 353-358 (2011).
- 822 [59] Bak, P., Tang, C., Wiesenfeld, K. Self-organized criticality: an explanation  
823 of 1/f noise. *Phys Rev Lett* **59**, 381-384 (1987).
- 824 [60] Phillips, J.C. Scaling and self-organized criticality in proteins I. *Proc Natl*  
825 *Acad Sci USA* **106**, 3107-3112 (2009).

- 826 [61] Phillips, J.C. Scaling and self-organized criticality in proteins II. *Proc Natl*  
827 *Acad Sci USA* **106**, 3113-3118 (2009).
- 828 [62] Morett, M. Self-organized critical model for protein folding. *Physica A* **390**,  
829 3055-3059 (2011).
- 830 [63] Phillips, J.C. Self-organized criticality in proteins: Hydropathic roughening  
831 profiles of G-protein-coupled receptors. *Phys Rev E* **87**, 032709 (2013).
- 832 [64] Zhou, R., Silverman, B.D., Royyuru, A.K., Athma, P. Spatial profiling of  
833 protein hydrophobicity: Native vs. decoy structures. *Proteins* **52**, 561-572  
834 (2003).
- 835 [65] Xenakis, M.N., Kapetis, D., Yang, Y. et al. Cumulative hydropathic topol-  
836 ogy of a voltage-gated sodium channel at atomic resolution. *Proteins*, 1319-  
837 1328, (2020).
- 838 [66] Xenakis, M.N., Kapetis, D., Yang, Y. et al. Non-extensivity and criticality  
839 of atomic hydropathicity around a voltage-gated sodium channel's pore; a  
840 modeling study. Under review in *J Biol Phys*.
- 841 [67] R Core Team *R: A language and environment for statistical computing*.  
842 R Foundation for Statistical Computing, Vienna, Austria. [http://www.](http://www.R-project.org/)  
843 [R-project.org/](http://www.R-project.org/) (2014).
- 844 [68] Humphrey, W., Dalke, A., Schulten K. VMD-Visual Molecular Dynamics.  
845 *J Molec Graph* **14**, 33-38 (1996).
- 846 [69] Loss, R.D. Atomic weights of the elements 2001 (IUPAC technical report).  
847 *Pure Appl Chem* **73**, 667-683 (2001).
- 848 [70] Bondi, A. Van der Waals volumes and radii. *J Phys Chem* **68**, 441-51  
849 (1964).
- 850 [71] Rowland, R.S., Taylor, R. Intermolecular nonbonded contact distances in  
851 organic crystal structures: comparison with distances expected from van der  
852 Waals radii. *J Phys Chem* **100**, 7384-7391 (1996).
- 853 [72] Smart, O.S., Neduvilil, J.G., Wang, X., Wallace, B.A., Sansom, M.S.P.  
854 HOLE: A program for the analysis of the pore dimensions of ion channel  
855 structural models. *J Mol Graph* **14**, 354-360 (1996).
- 856 [73] Kahm, M., Hasenbrink, G., Lichtenberg-Fraté, H., Ludwig, J., Kschischo  
857 M. Fitting Biological Growth Curves with R. *J Stat Softw* **33**, 1-21 (2010).
- 858 [74] Zwietering, M.H., Jongenburger, I., Rombouts, F.M., van't Riet, K. Mod-  
859 eling of the bacterial growth curve. *Appl Environ Microbiol* **56**, 1875-1881  
860 (1990).
- 861 [75] Blumberg, A.A. Logistic growth rate functions. *J Theoret Biol* **21**, 42  
862 (1968).

- 863 [76] Gompertz, B. On the nature of the function expressive of the law of human  
864 mortality, and on a new mode of determining the value of life contingencies.  
865 *Philos Trans R Soc London* **115**, 513-585 (1825).
- 866 [77] Zwietering, M.H., Jongenburger, I., Rombouts, F.M., van't Riet, K. Mod-  
867 eling of the Bacterial Growth Curve. *Appl Environ Microbiol* **56** 1875-1881  
868 (1990).
- 869 [78] Richards, F.J. A flexible growth function for empirical use. *J Exp Bot* **10**,  
870 290-300 (1959).
- 871 [79] E., Tjørve, Tjørve, K.M.C. A unified approach to the Richards-model fam-  
872 ily for use in growth analyses: Why we need only two model forms. *J Theor*  
873 *Biol* **267**, 417-425 (2010).
- 874 [80] Eisenberg, D., Weiss, R.M., Terwilliger, T.C., Wilcox, W. Hydrophobic  
875 moments and protein structure. *Faraday Symp Chem Soc* **17**, 109-120 (1982).
- 876 [81] Kapcha, L.H., Rossky, P.J. A simple atomic-level hydrophobicity scale re-  
877 veals protein interfacial structure. *J Mol Biol* **426**, 484-498 (2014).
- 878 [82] Gromiha, M.M., Oobatake, M., Kono, H., Uedaira, H., Sarai, H. Role  
879 of structural and sequence information in the prediction of protein stability  
880 changes: comparison between buried and partially buried mutations. *Protein*  
881 *Eng* **12**, 549-555 (1999).
- 882 [83] Gromiha, M.M. Factors influencing the thermal stability of buried protein  
883 mutants. *Polymer* **44**, 4061-4066 (2003).
- 884 [84] Robin, X., Turck, N., Hainard, A., Tiberti, N., Lisacek, F., Sanchez, J.,  
885 Müller, M. pROC: an open-source package for R and S+ to analyze and  
886 compare ROC curves. *BMC Bioinformatics*, **12**, 77 (2011).
- 887 [85] Following [66], let us consider the case of a missense SCN9A mu-  
888 tation expressed in the perturbation form of  $N(\mathbf{p}_{crit.}, l_\alpha(\mathbf{p}_{crit.})) \rightarrow$   
889  $N(\mathbf{p}_{crit.}, l_\alpha(\mathbf{p}_{crit.})) + \epsilon(\mathbf{p}_{crit.}, l_\alpha(\mathbf{p}_{crit.}))$ , with  $\epsilon(\mathbf{p}_{crit.}, l_\alpha(\mathbf{p}_{crit.}))$  being a  
890 small-amplitude perturbation source describing addition and/or removal  
891 of a small number of atoms due mutation translation. Then, HICIS  
892 is regulated according to  $h_z^{(1)}(\mathbf{p}_{crit.}, l_\alpha(\mathbf{p}_{crit.})) + \zeta(\mathbf{p}_{crit.}, l_\alpha(\mathbf{p}_{crit.})) \sim$   
893  $l_\alpha(\mathbf{p}_{crit.})^{\gamma(\mathbf{p}_{crit.})} \cdot (N(\mathbf{p}_{crit.}, l_\alpha(\mathbf{p}_{crit.})) + \epsilon(\mathbf{p}_{crit.}, l_\alpha(\mathbf{p}_{crit.})))$  with  $\gamma(\mathbf{p}_{crit.}) =$   
894  $\gamma_{partI}(\mathbf{p}_{crit.})$  for  $s(\mathbf{p}_{crit.}) < l_\alpha(\mathbf{p}_{crit.}) \leq \xi(\mathbf{p}_{crit.})$  and  $\gamma(\mathbf{p}_{crit.}) =$   
895  $\gamma_{partII}(\mathbf{p}_{crit.})$  for  $\xi(\mathbf{p}_{crit.}) < l_\alpha(\mathbf{p}_{crit.}) \leq o(\mathbf{p}_{crit.})$  so that the HICIS law  
896 described by r1 remains intact around the critical point.
- 897 [86] Heyne, H.O., Baez-Nieto, Iqba, S. et al. A machine learning method can  
898 predict loss- versus gain-of-function effects of human genetic variants in  
899 disease-associated ion channels. *Sci Transl Med* **12**, 556 (2020).

- 900 [87] Tsuchiya, M., Giuliani, A., Hashimoto, M., Erenpreisa, J., Yoshikawa,  
901 K. Self-Organizing Global Gene Expression Regulated through Criticality:  
902 Mechanism of the Cell-Fate Change. *PLoS ONE* **11**, 12 (2016).
- 903 [88] Pavlos, G.P., Karakatsanis, L.P., Iliopoulos, A.C. et al. Measuring com-  
904 plexity, nonextensivity and chaos in the DNA sequence of the Major Histo-  
905 compatibility Complex. *Physica A* **438**, 188-209 (2015).
- 906 [89] Furusawa, C., Kaneko, K. Adaptation to optimal cell growth through self-  
907 organized criticality. *Phys. Rev. Lett.* **108**, 208103 (2012).
- 908 [90] Janina, H., Gross, T. Self-organized criticality as a fundamental property  
909 of neural systems. *Front Syst Neurosci* **8**, 166 (2014).
- 910 [91] Beggs, J.M. The criticality hypothesis: How local cortical networks might  
911 optimize information processing. *Phil Trans R Soc A* **366**, 329-343 (2008).
- 912 [92] Bertschinger, N., Natschläger, T. Real-time computation at the edge of  
913 chaos in recurrent neural networks. *Neural Comput* **16**, 1413-1436 (2004).
- 914 [93] Kinouchi, O., Copelli, M. Optimal dynamical range of excitable networks  
915 at criticality. *Nat Phys* **2**, 348-351 (2006).
- 916 [94] Watkins, N.W., Pruessner, G., Chapman, S.C. et al. 25 Years of Self-  
917 organized Criticality: Concepts and Controversies. *Space Sci Rev* **198**, 3-44  
918 (2016).
- 919 [95] Shen, H., Liu, D., Wu, K., Lei, J., Yan, N. Structures of human Na<sub>v</sub>1.7  
920 channel in complex with auxiliary subunits and animal toxins. *Science* **363**,  
921 1303-1308 (2019).
- 922 [96] Karczewski, K.J., Francioli, L.C., Tiao, G. et al. Variation across 141,456  
923 human exomes and genomes reveals the spectrum of loss-of-function intoler-  
924 erance across human protein-coding genes. *bioRxiv*, 531210 (2019).
- 925 [97] Toffano, A., Chiarot, G., Zamuner, S. et al. Computational Pipeline to  
926 probe NaV1.7 gain-of-functions variants in neuropathic painful syndromes.  
927 *Sci Rep* **10**, 17930 (2020).

# Figures

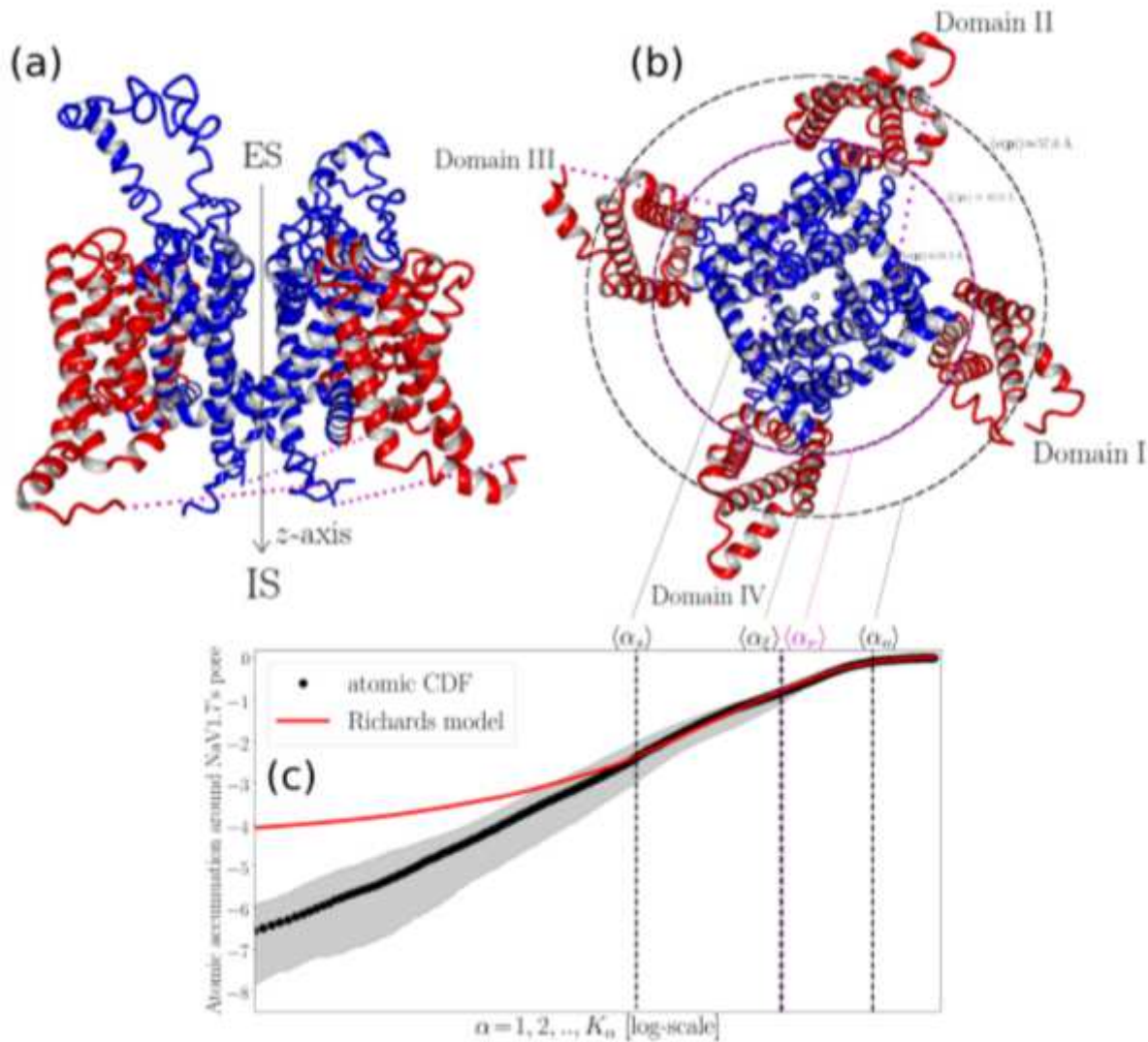


**Figure 1**

Atomic accumulation around NaV1.7's pore. (a),(b) Cartoon illustration of the NaV1.7 human channel (side and top views). The atomic environment around the pore is partitioned into three consecutive domains; a lag domain, an inflection domain, and an asymptote domain. The upper boundaries of the lag domain, of the pre-inflection domain and of the post-inflection domain are also shown in terms of their statistical representations  $\langle \alpha_L \rangle$ ,  $\langle \alpha_I \rangle$ ,  $\langle \alpha_A \rangle \approx \langle \alpha \rangle$  and  $\langle \alpha_0 \rangle$ , respectively. Helical structures in (a),(b) forming the PMs and the VSs are colored with red and blue color, 268 respectively. (c), Traces of statistical representations of the normalized (with respect to  $N_c$ ) atomic CDF,  $\langle N(p, \alpha(p)) \rangle_\alpha$ , and of its best-fitted Richards model  $\langle n(p, \alpha(p)) \rangle_\alpha$  are plotted in log-scale with shaded areas around  $\langle N(p, \alpha(p)) \rangle_\alpha$  indicative of 95% confidence intervals. Statistical representations of scalars are calculated according to SM, S6.

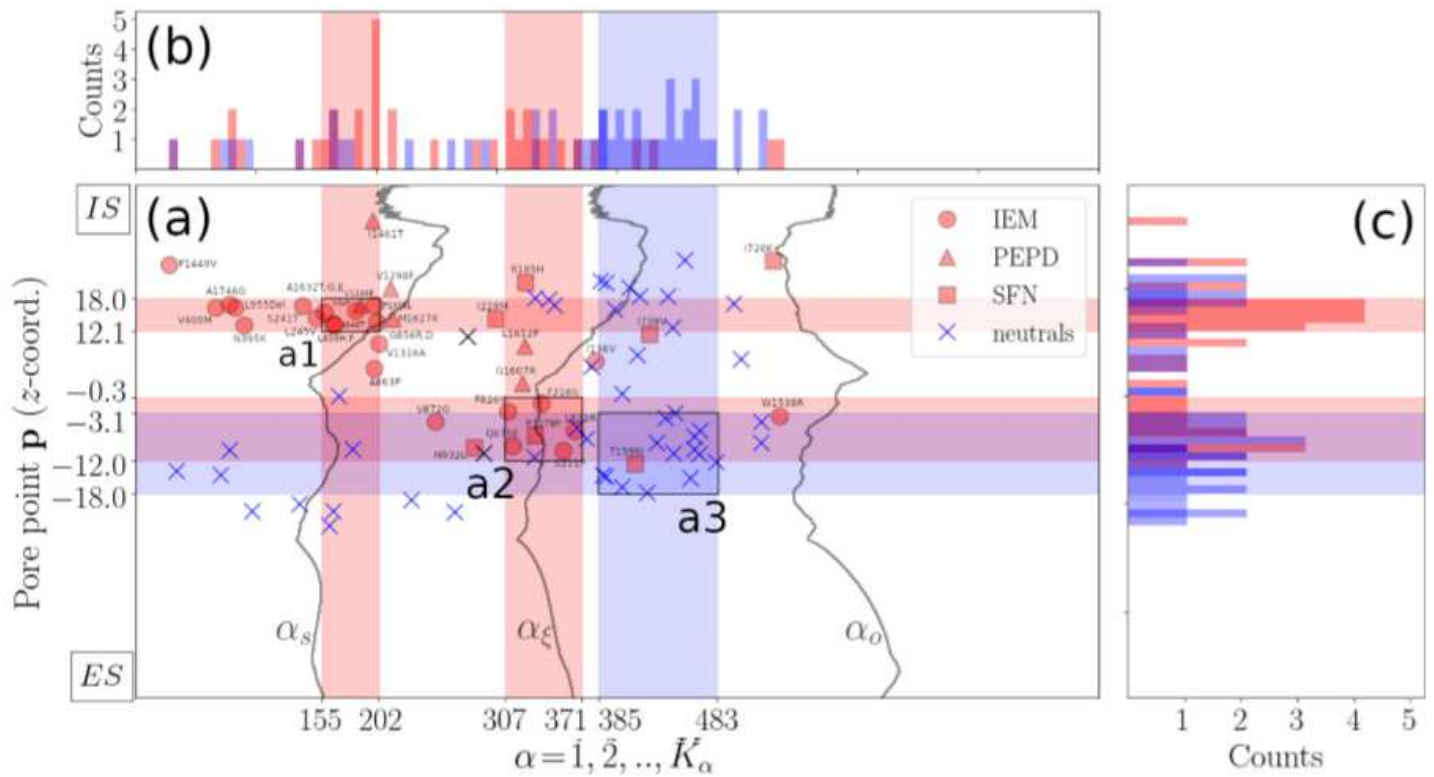


**Figure 2**

Geometrical mapping of missense SCN9A-gene mutation sites. (a), Two sets of missense SCN9A-gene mutation are employed; a pain-related set containing IEM, PPD and SFN mutation sites and a neutral set containing mutation sites not related to pain disease (SM, S3). Lines  $\alpha_s$ ,  $\alpha_\xi$  and  $\alpha_o$  highlight the boundaries among consecutive domains. Map areas "a1", "a2" and "a3" indicate maximizations in density of mutation sites. (b), Histogram of mutation sites along  $\alpha$ -direction. (c), Histogram of mutation sites along  $p$ -direction. Red- and blue-colored histograms account for distribution of pain-related and neutral mutation sites, respectively.

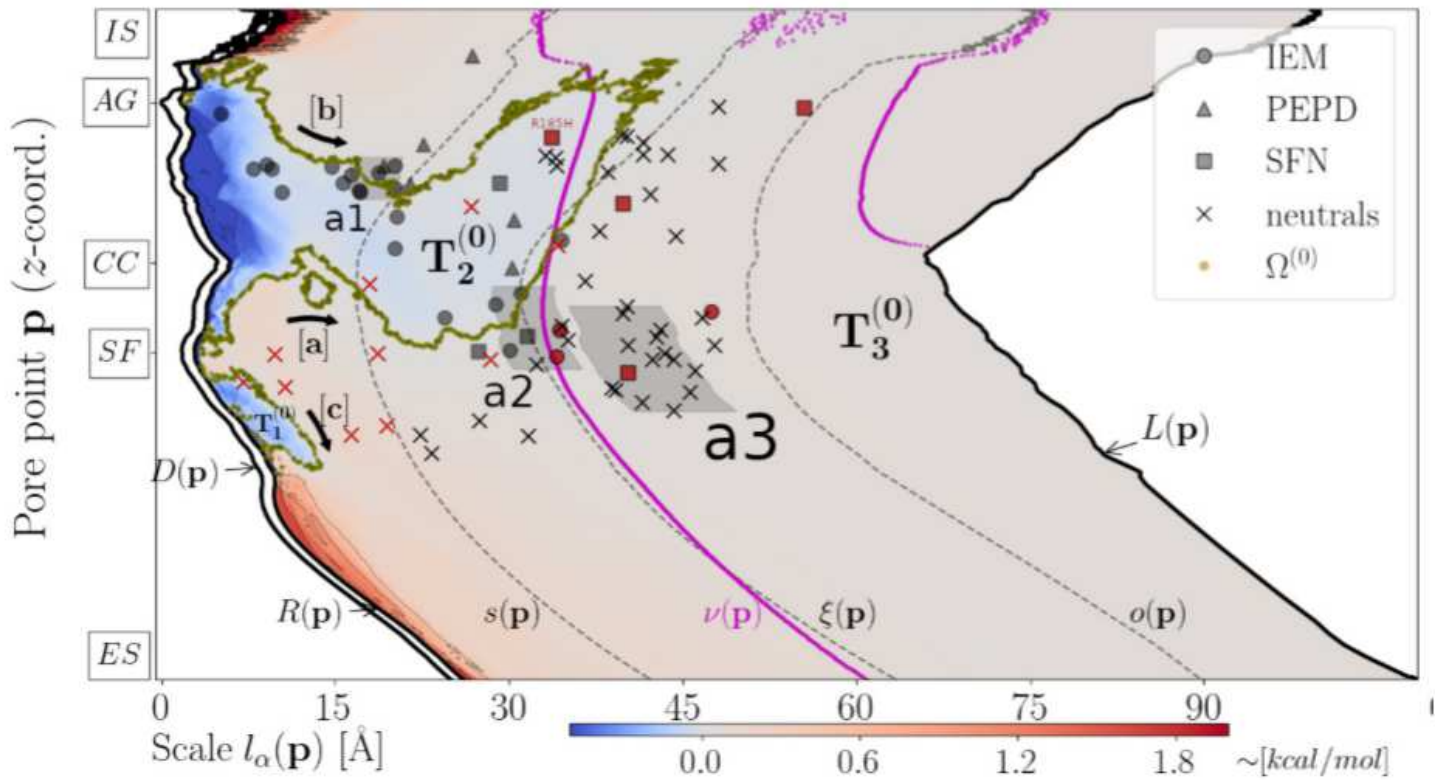


**Figure 3**

Spatial profile of the hydrophatic density around NaV1.7's pore. Contour map of the hydrophatic density pore function,  $m^{(0)}(p, l_\alpha(p))$ , for  $p \in P$  and  $\alpha=1,2,\dots,K_\alpha=800$ . Blue and red color contour domains represent hydrophobic and hydrophilic domains around the pore, respectively. Black lines  $R(p)$ ,  $\xi(p)$  and  $L(p)$  depict geometrical pore characteristics. Magenta dashed line  $\nu(p)$  represents the PMs-VSs spatial transition. Dashed black lines  $s(p)$ ,  $\xi(p)$  and  $o(p)$  account for the boundaries between different domains (see Methods). Zero-crossing points of  $m^{(0)}(p, l_\alpha(p))$  collected in  $\Omega^{(0)}$  describe the boundaries among hydrophatic domains  $T^{(0)}_1$ ,  $T^{(0)}_2$  and  $T^{(0)}_3$ . Pain-related and neutral mutation sites are represented by different symbols (see Legend). Mutations sites highlighted with red color correspond to misclassified events. Grey-shaded areas "a1", "a2" and "a3" highlight map areas where map density of mutation sites maximizes. Note: The designations employed and the presentation of the material on this map do not imply the expression of any opinion whatsoever on the part of Research Square concerning the legal status of any country, territory, city or area or of its authorities, or concerning the delimitation of its frontiers or boundaries. This map has been provided by the authors.

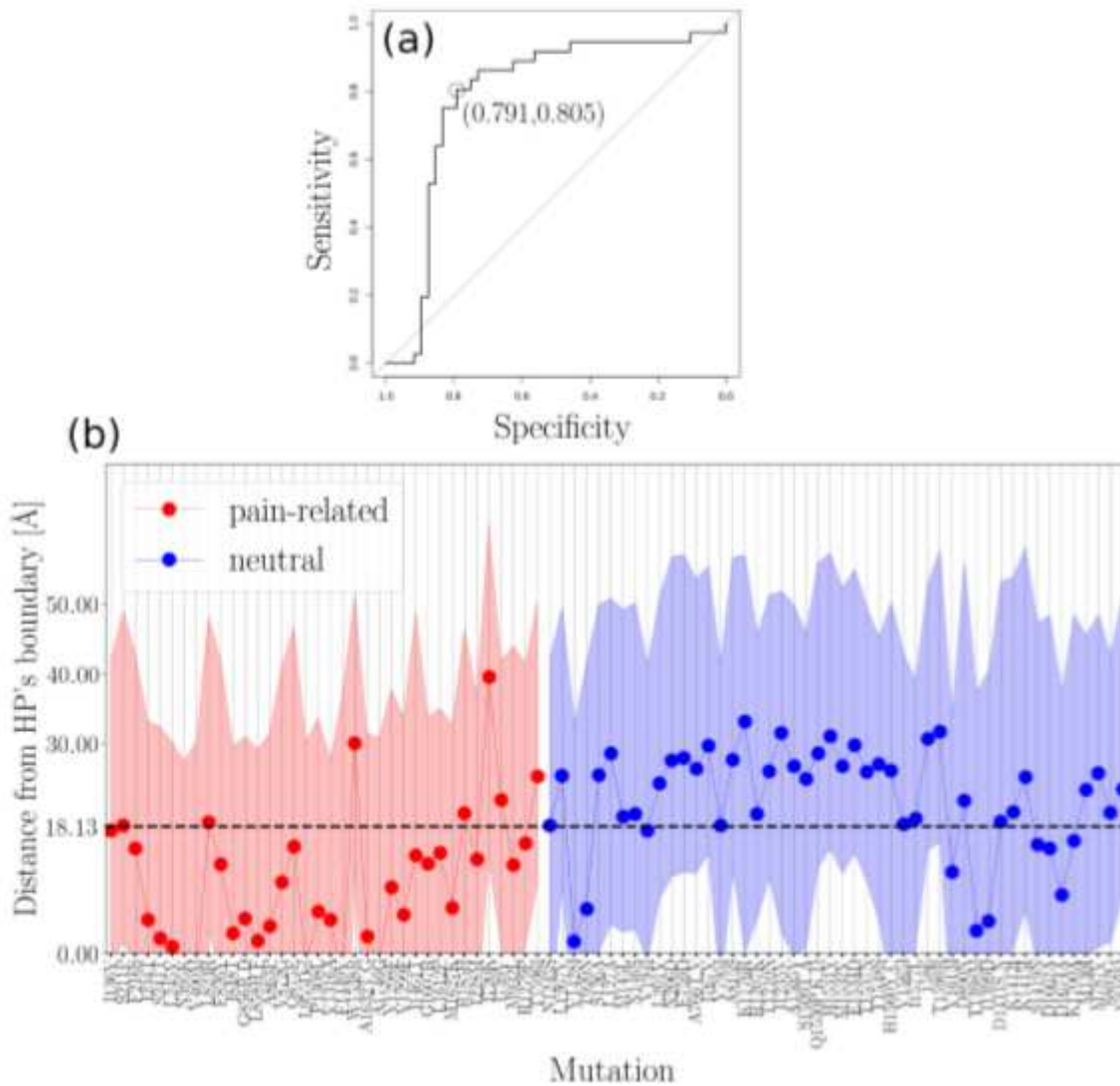


**Figure 4**

Binary classification of NaV1.7 variants based on their distance from the HP's boundary. (a), ROC curve constructed based on the HP's-boundarydistance data (for construction of data set see SM, S8). Optimal threshold value corresponds to specificity and sensitivity values of 0.791 and 0.805, respectively. Area under ROC curve is 0.787. (b), Visualization of ROC curve data. Optimal threshold value 18.13 Å is marked with black dashed line. Shaded area around distance values indicates the 95% confidence intervals. ROC curve is constructed in R [67] by using the pROC package [84].

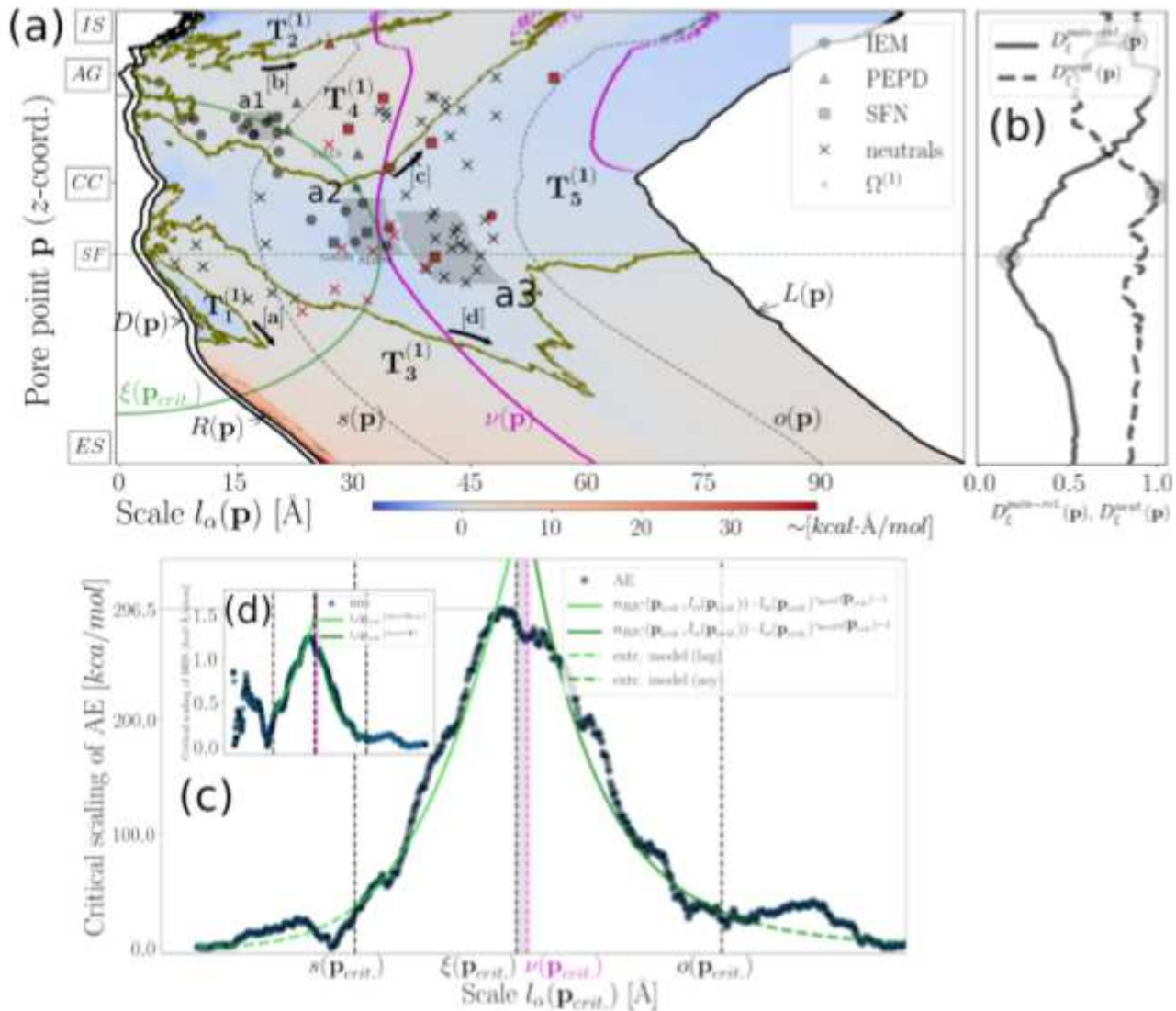


**Figure 5**

Spatial profile of HIIIS along NaV1.7's pore. (a), Contour map of HIIIS axial part,  $m(1) z(p, l_\alpha(p))$ , for  $p \in P$  and  $\alpha = 1, 2, \dots, K_\alpha = 800$ . Blue and red color contour domains represent configurations of  $\sim m(1) z(p, l_\alpha(p))$  with orientation "out" and "in", respectively. Black lines  $R(p)$ ,  $\bar{R}(p)$  and  $L(p)$  depict geometrical pore characteristics. Magenta dashed line  $v(p)$  represents the PMs-VSs spatial transition. Dashed black lines  $s(p)$ ,  $\xi(p)$  and  $o(p)$  account for the boundaries between different domains.  $\xi(p_{crit.})$  represents the critical radius. Black arrows [a], [b], [c], [d] and [e] indicate the clustering behavior of the zero-crossing points of  $m(1) z(p, l_\alpha(p))$  collected in  $\Omega(1)$  describing boundaries among contour domains  $T(1) 1$ ,  $T(1) 2$ ,  $T(1) 3$ ,  $T(1) 4$  and  $T(1) 5$ . Mutations sites highlighted with red color correspond to misclassified events. Grey-shaded areas "a1", "a2" and "a3" highlight map areas where map density of mutation sites maximizes. (b), Distance between inflection points and mutation sites along the pore is also plotted in terms of the normalized (with respect to maximum value) statistical representations  $\bar{D}_{path}$ .  $\xi(p)$  and  $\bar{D}_{cont}$ .  $\xi(p)$ , respectively. (c), Power-law scaling of HIIIS axial part for  $p_{crit.} = (p_x \approx 0, p_y \approx 0, p_z = -12.1)$ . The best-fitting first-part-inflection-domain and second-part-inflection-domain power-law approximations

are also plotted with mean absolute relative fitting errors being  $0.09 \pm 0.01$  and  $0.15 \pm 0.03$ , respectively. (d), Power-law-like behavior of AE,  $U(p, l(p))$  for  $p_{crit.} = (p_x \approx 0, p_y \approx 0, p_z = -12.1)$ . First- and second-part-inflection-domain modeling approximations of AE are also plotted with their mean absolute relative modeling errors being  $0.11 \pm 0.02$  and  $0.14 \pm 0.03$ , respectively. AE model extrapolation toward the lag-domain  $l(p) \leq s(p)$  and the asymptote-domain  $l(p) > o(p)$  result in a mean absolute relative fitting error of  $6.06 \pm 16.0$  and  $1.55 \pm 6.39$ , respectively. Richards model parameters used for modeling AE are  $\{A(p_{crit.}) = 1.03, t(p_{crit.}) = 0.03, s(p_{crit.}) = 18.16, \sim q(p_{crit.}) = 0.47\}$ . Note: The designations employed and the presentation of the material on this map do not imply the expression of any opinion whatsoever on the part of Research Square concerning the legal status of any country, territory, city or area or of its authorities, or concerning the delimitation of its frontiers or boundaries. This map has been provided by the authors.

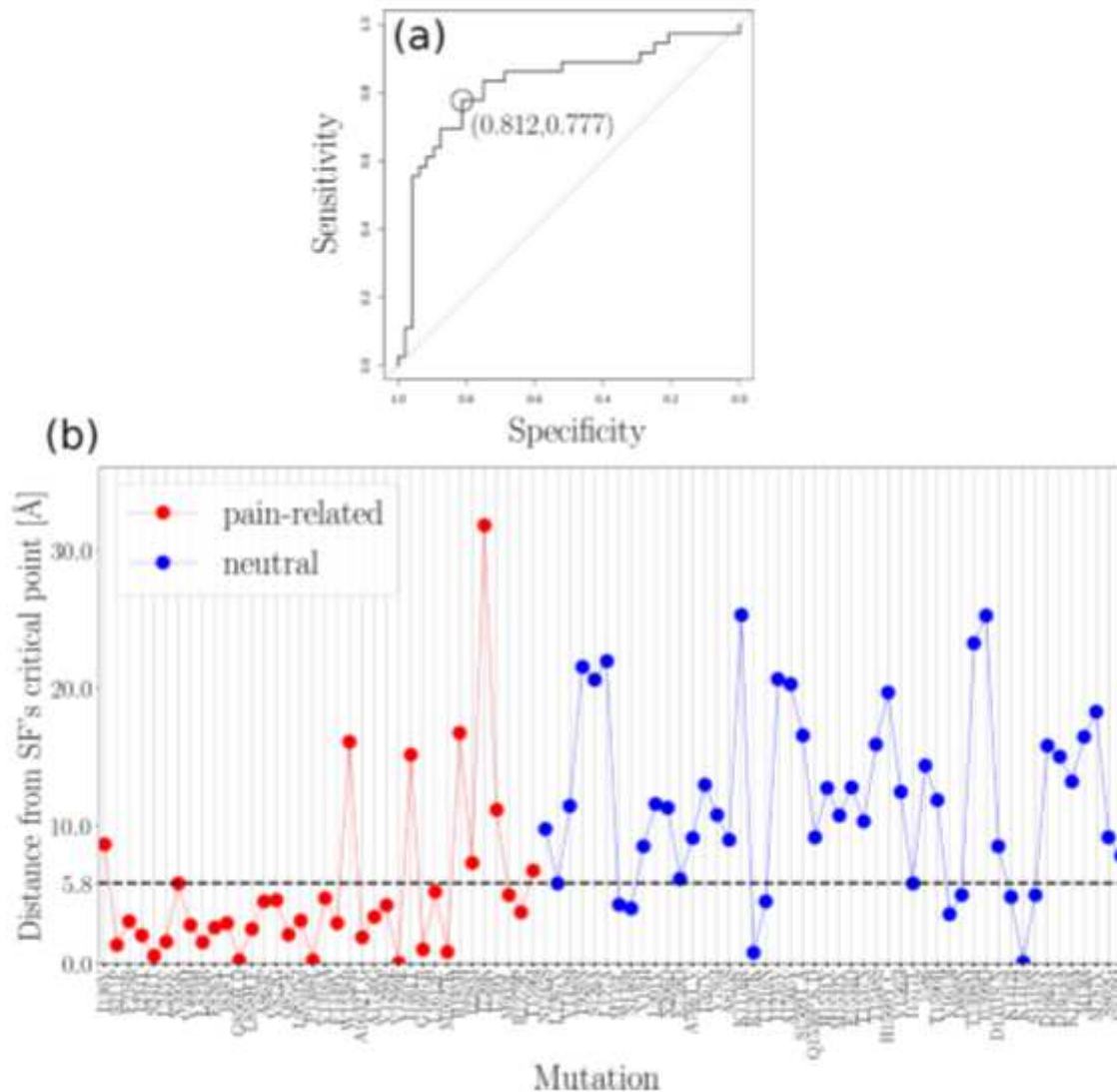


**Figure 6**

Binary classification of NaV1.7 variants based on their distance from SF's critical point. (a), ROC curve constructed based on SF's-critical-point distance data (for construction of data set see SM, S8). Optimal threshold value 5.8 Å corresponds to specificity and sensitivity values of 0.812 and 0.777, respectively.

Area under ROC curve is 0.824. (b), Visualization of ROC curve data. Optimal threshold value 5.8 Å is marked with black dashed line. ROC curve is constructed in R [67] by using the pROC package [84].

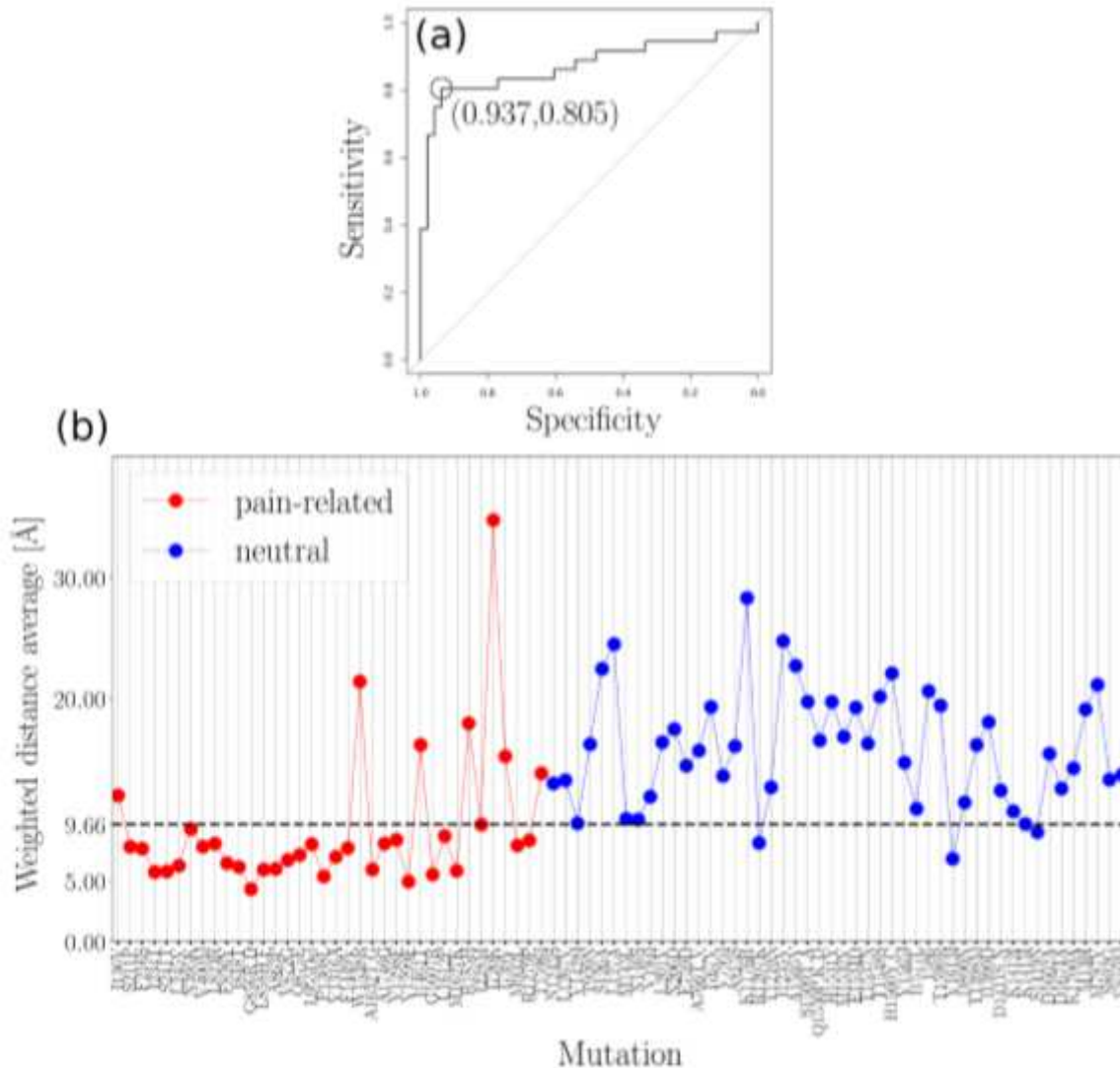


**Figure 7**

Binary classification of NaV1.7 variants based on the weighted distance average. (a), ROC curve constructed based on weighted distance data (for construction of data set see SM, S8). Optimal threshold value 9.6 Å corresponds to specificity and sensitivity values of 0.805 and 0.937, respectively. Area under ROC curve is 0.872. (b), Visualization of ROC curve data. Optimal threshold value 9.6 Å is marked with black dashed line. ROC curve is constructed in R [67] by using the pROC package [84].

## Supplementary Files

This is a list of supplementary files associated with this preprint. Click to download.

- [XenakisetalSuppl.pdf](#)